# Active chaotic mixing of yield stress fluids in an open channel flow

Yann Moguen, Eliane Younes, Kamal El Omari, Cathy Castelain, Yves Le Guer, Teodor Burghelea

# Active chaotic mixing of yield stress fluids in an open channel flow

Yann Moguen[1], Eliane Younes[2], Kamal El Omari[3], Cathy Castelain[2], Yves Le Guer[1] and Teodor Burghelea[2*]

[1] Laboratoire SIAME, Université de Pau et des Pays de l'Adour, E2S UPPA, Pau, France.
[2*]Laboratoire de Thermique et Énergie de Nantes, LTeN, UMR 6607, Nantes Université , CNRS, Rue Christian Pauc, Nantes, 44306, Country.
[3]PIMENT laboratory, University of Reunion Island, 40 Av. Soweto, Saint-Pierre, 97455, La Réunion, France.
[4]IMT Nord Europe, Institut Mines Télécom, University of Lille, Center for Energy and Environment, Lille, F-59000 , France.

*Corresponding author(s). E-mail(s): Teodor.Burghelea@univ-nantes.fr;
Contributing authors: yann.moguen@univ-pau.fr; Eliane.Younes@univ-nantes.fr; kamal.el-omari@univ-reunion.fr; Cathy.Castelain@univ-nantes.fr; yves.leguer@univ-pau.fr;

**Abstract**

A numerical investigation of active mixing of yield stress fluids using a mixer recently proposed in Ref. [El Omari et al(2021)El Omari, Younes, Burghelea, Castelain, Moguen, and Le Guer] and tested experimentally with Newtonian fluids [Younes et al(2022)Younes, Moguen, El Omari, Burghelea, Le Guer, and Castelain] is presented is presented. As the Bingham number (defined by the ratio of the yield stress to the viscous stress) is increased past a critical value $\mathrm{Bn}_{\mathbf{bulk}}^{\mathbf{crit}} \approx \mathbf{5}$, a dramatic decrease of both the efficiency of the mixing process and of the homogeneity of the final mixture is observed. Further physical insights into this observation are obtained by a systematic analysis of the space-time dynamics of the flow fields in both Eulerian and Lagrangian frames. The numerical results show that the cascade of the passive scalar fluctuations from the wave

numbers associated to the integral scale at which the passive scalar is injected down to the diffusive scale is obstructed by the emergence of a supplemental space scale associated to the characteristic size of the un-yielded material elements. The study is complemented by the discussion of two plausible solutions for alleviating the dramatic loss of mixing efficiency induced by the viscoplastic fluid behavior. .

**Keywords:** yield stress materials, laminar chaotic advection, mixing, Finite Time Lyapunov exponents

# 1 Introduction

Yield stress materials represent a distinct class materials that do not flow (or *"yield"*) unless subjected to a critical stress called *"yield stress"*. Such materials commonly referred to in the daily life as *"pasty materials"* are characterized by a physically complex microscopic scale structure that tends to resist deformation prior to yielding.

The macroscopic yield stress behavior may emerge from a variety of distinct chemical identities and micro-structural configurations. Thus, one commonly observes a similar macroscopic yield stress behavior in materials with significantly different microscopic structures such as emulsions, foams, colloidal gels, physical gels, suspensions of micro-algae, mud, cement, magma etc. These materials which seem homogeneous at the macroscopic scale and exhibit an yield stress behavior can be composed of several phases (the emulsions for example) which makes their macroscopic behavior very sensitive to various physico-chemical parameters (*e.g.* temperature, $pH$). According to the bibliographic database Scopus, during the past two decades the interest in the physics of yield stress materials has increased exponentially with time. There exist at least two important reasons underlying this fact. First, from a practical standpoint, such materials are relevant to a number of key modern industrial sectors including (but not limited to) food, oil field, cosmetic, pharmaceutical, construction. Second, from a fundamental standpoint, understanding the physical behavior of yield stress materials in a broad sense posses formidable challenges that can only be addressed via an inter-disciplinary approach, *i.e.* by combining tools of several distinct research fields: fluid mechanics, rheology, nonlinear dynamics and critical phenomena, chemical physics, applied mathematics etc.

The current progress in understanding the flows of yield stress materials has been systematically described in several review papers, [Nguyen and Boger(1992), Bonn and Denn(2009), Balmforth et al(2014)Balmforth, Frigaard, and Ovarlez, Coussot(2014), Bonn et al(2017)Bonn, Denn, Berthier, Divoux, and Manneville, Frigaard(2019)].

A problem that is fundamental to fluid mechanics and of an undisputed practical relevance relates to the efficient mixing of two viscous fluid streams. To our best knowledge, the efficient mixing of yield stress materials is currently a largely unexplored area which sets the global motivation of the present contribution.

The mixing of Newtonian fluids may occur mainly due to three mechanisms which, while physically different, they all break the time reversal symmetry (in either an Eulerian or a Lagrangian frame of reference) in the flow. The first and perhaps the most natural is the molecular diffusion. This mechanism is often not very effective particularly in the cases when the species to be mixed have a large molar mass and/or the mixing is expected to take place over extended space scales as is the case for the vast majority of practical applications. It is rather obvious that in the case of yield stress materials this mechanism is practically switched off. A second physical mechanism able to break the time-reversal symmetry of the flow relates to the inertial turbulence: in large Reynolds number flows the inertial nonlinearity leads to the emergence of secondary flows that are able to mix efficiently two distinct fluid streams. In the case when the mixing of yield stress materials is envisaged, this mechanism too may turn un-practical for at least two reasons. First, triggering an inertial nonlinearity in highly viscous materials with yield stress requires significant energy inputs which is certainly undesirable for many processing operations. Second, as most of the yield stress materials are *"soft"* from a textural viewpoint, triggering inertial instabilities is associate to large Reynolds stresses that may presumably lead to mechanical degradation of the soft structure thus altering the properties of the final mixture.

A third physical mechanism able to break the time reversal symmetry and trigger mixing in the flow is the so called *"laminar chaotic advection"*.

Laminar chaotic advection is a physical phenomenon that allows complex trajectories of passive particles to be obtained for a relatively simple regular flow even at very low Reynolds number. This particular feature of chaotic laminar flows makes them more attractive than their inertial counterpart, in terms of energy consumption as it requires no significant inertial contributions. [Aref(1984)] was the first to establish the link between the ability of dynamical systems to produce chaotic trajectories and the use of this property for fluid mixing. Almost at the same time, [Ottino(1989)] linked the stretching and folding properties of fluid elements (filaments in $2D$, sheets in $3D$) to the notion of chaotic fluid mixing. From a fluid mechanics standpoint, while discussing the possibility of triggering the laminar chaotic advection, it is necessary to distinguish $2D$ flows from $3D$ flows.

The equations of motion of particles of coordinates $(x, y)$ advected by a $2D$ (planar) incompressible flow field $(v_x, v_y)$ have a Hamiltonian simplectic form:

$$v_x = \frac{dq}{dt} = \frac{\partial \mathcal{H}}{\partial p}, \tag{1}$$

$$v_y = \frac{dp}{dt} = -\frac{\partial \mathcal{H}}{\partial q}, \tag{2}$$

$$q = x, \quad p = y, \quad \mathcal{H}(q,p) = \Psi(x,y), \tag{3}$$

where the Hamiltonian $\mathcal{H}$ is just the stream function $\Psi$. Although generally credited to [Aref(1984)], the Hamiltonian approach to fluid mechanics predates his discovery of the laminar chaotic by roughly four decades and goes back to the un-published theory of turbulence of Lars Onsager. Thus, Lars Onsager modelled turbulent flows by a system of $N$ interacting vortices and writing the Hamiltonian of the system in terms of stream function allowed him to extensively use tools of non equilibrium thermodynamics and derive an expression for the turbulent spectrum of velocity (independently from A.N. Kolmogorov). An enlightening and systematic historical review of the un-published work of Lars Onsager on inertial turbulence including extracts from his hand written or typed notes/correspondence may be found in Ref. [Eyink and Sreenivasan(2006)].

For a time-independent streamfunction $\Psi = \Psi(x,y)$ the fluid particles follow streamlines that are frozen in time and their trajectories are regular. The system is said to be *"integrable"* in this case. On the contrary, when the streamfunction is time dependent $\Psi = \Psi(x,y,t)$, the Hamiltonian system becomes generally non-integrable and individual particle trajectories can become chaotic in a Lagrangian frame of reference. For $2D$ flows it is thus necessary to introduce an unsteady forcing (time dependence) of the flow in order to obtain chaotic advection. One way to trigger laminar chaotic advection is to impose a time dependent flow forcing at the walls (*e.g.* a time periodic forcing). For a $3D$ flow, the additional degree of freedom brought by the third dimension removes the unsteadiness constraint needed to generate chaotic trajectories . This is the case of the $3D$ herringbone mixer proposed by Stroock and coworkers, [Stroock et al(2002)Stroock, Dertinger, Ajdari, Mezić, Stone, and Whitesides]. In an unsteady $2D$ flow the fluid particles have the possibility to *"jump"* from one streamline to another. It is therefore legitimate to question the possibility of obtaining chaotic trajectories during flows of yield stress materials where yielded material elements typically coexist with un-yielded ones.

Another distinctive feature of flows in a regime of laminar chaotic advection relates to their spatial smoothness. Thus, mixing by laminar chaotic advection is directly related to the so called Batchelor regime of mixing observed in the viscous-convective range of wave numbers, $k_K < k < k_B$, [Batchelor(1959), Kraichnan(1968)]. Here $k_K$ and $k_B$ are the Kolmogorov and the Batchelor wave numbers, respectively. In spite of its undisputed relevance to the mixing problem, there exist rather few theoretical ([Duplat and Villermaux(2008), Fereday et al(2002)Fereday, Haynes, Wonhas, and Vassilicos, Fereday and Haynes(2004)]) and experimental ([Jullien et al(2000)Jullien, Castiglione, and Tabeling, Jullien(2003), Burghelea et al(2004a)Burghelea, Segre, Bar-Joseph, Groisman, and Steinberg,

Burghelea et al(2004b)Burghelea, Segre, and Steinberg, Burghelea(2005)]) studies of the Batchelor regime of mixing. The flow fields corresponding to the Batchelor regime of mixing are spatially smooth and random in time. The chaotic mixing realised by such flows is characterised by an exponential decay of the variance of the passive scalar with time and an algebraically decaying spectrum of the passive scalar fluctuations, $P \propto k^{-1}$.

As compared to the much better documented Newtonian case briefly discussed above, the presence of yield stress adds several layers of complexity to the mixing problem. While in a solid state, material elements practically do not mix. Thus, in order for the mixing to occur in yield stress materials, such materials need to yield first. This means that the yielding behavior and the mixing can not be easily decoupled. A second layer of complexity relates to the fact that for most flow configurations of a mixing device, the stress distribution is spatially in-homogeneous: various regions of the flow are typically subjected to different stresses. Thus, generally speaking, the yielding process is expected to be spatially in-homogeneous, i.e solid and fluid material elements co-exist within the same mixing device. Third, even in an yielded state, the viscoplastic material elements are typically rather viscous (with apparent viscosities ranging from a hundred to a thousand times that of the pure water) and, as already discussed for the Newtonian case, efficient mixing protocols need to be proposed in such case.

The subject of chaotic laminar advection or chaotic mixing in yield stress fluids has been little discussed in the literature. To our knowledge, only few studies exist: a study of [Arratia et al(2006)Arratia, Kukura, Lacombe, and Muzzio] who have investigated the mixing of shear-thinning fluids with yield stress in a classical $3D$ stirred tank, that of which deals with and that of the research group of P. Jop, [Wendell et al(2013)Wendell, Pigeonneau, Gouillart, and Jop, Boujlel et al(2016)Boujlel, Pigeonneau, Gouillart, and Jop] which deals with an $2D$ experimentally study of the rate of chaotic mixing in viscoplastic fluids by using a rod-stirring protocol in a rotating tank and a more recent one of [Lester and Chryss(2019)] that explores experimentally the topological mixing of viscoplastic non-Newtonian materials in a $3D$ continuous flow. While there seems to exist a general consensus on the fact that the presence of yield stress inhibits the chaotic mixing, the physical mechanisms underlying this fact remain elusive.

In a broad sense, the central scope of the present contribution relates to understanding the dynamics of the active mixing of yield stress materials via *laminar chaotic advection* in a rotating arc-wall mixer initially introduced numerically in Ref. [El Omari et al(2021)El Omari, Younes, Burghelea, Castelain, Moguen, and Le Guer] and experimentally in Ref. [Younes et al(2022)Younes, Moguen, El Omari, Burghelea, Le
The tested fluids were Newtonian.

Several fundamental aspects concerning the mixing of the yield stress materials by *laminar chaotic advection* will be addressed through the paper:

1. The role of yield stress on the space-time dynamics of a passive tracer in the presence of low molecular diffusion (the large Péclet number limit). A particular attention will be devoted to assessing the relationship between the mixing efficiency and the yield stress.
2. The role of yield stress on the Eulerian flow structure and the dynamics of solid and fluid material elements.
3. The coupling between the yield stress behavior and the Lagrangian dynamics of the flow.

The paper is organised as follows. The numerical setup is described in Sec. 2. The results of the numerical simulations are discussed in Sec. 3. The dramatic role of the yield stress on the efficiency of the mixing process is highlighted in Sec. 3.1. An Eulerian characterisation of the space-time dynamics of the random flows for various magnitudes of the yield stress is presented in Sec. 3.2. The Eulerian flow characterisation is complemented by a systematic Lagrangian analysis in terms of statistics of particle trajectories, residence times and maps of the Finite Time Lyapunov exponents, Sec. 3.3. Finally, two distinct solutions able to alleviate the dramatic loss of the efficiency of the mixing process due to the viscoplastic behavior of the fluid are discussed in Sec. 4. The paper closes with a summary of the main conclusions of the study, Sec. 5.

# 2 Numerical setup

## 2.1 Flow geometry, problem formulation

The rotating arc-walls mixer initially introduced in a recent contribution, [El Omari et al(2021)El Omari, Younes, Burghelea, Castelain, Moguen, and Le Guer] is schematically represented (in scale) in Fig. 1. It consists of a plane channel of total length $L = 5$ and the width $W = 1$, equipped with three rotating arc-walls. The arc-walls have a radius $R = 0.36$ and are centred in the points $O_{1-3}$. Each arc-wall protrudes within the main channel by the distance $\Delta = R$.

To induce mixing by *laminar chaotic advection*, an oscillatory forcing is imposed onto each of the three rotating arc-walls with angular velocities $\Omega_k = \Omega_k^0 \cos(ft + \delta_k)$, $k \in \{1, 2, 3\}$. The length of the *"active"* mixing zone, defined by the distance between the centres $O_{2,3}$ of the cylinders $C_{2,3}$, is $L_0 = 1.5$. The centre $O_1$ of the top cylinder $C_1$ is located at the middle distance between the centres of the bottom arc-walls $C_{2,3}$. The two arc-walls $C_{2,3}$ located on the bottom of the flow channel (see Fig. 1) rotate identically with $\Omega_2^0 = \Omega_3^0 = \Omega_0$ and $\delta_2 = \delta_3 = \pi/4$, whereas the top cylinder $C_1$ rotates with the same amplitude $\Omega_1^0 = \Omega_0$ but in an opposite direction $\delta_1 = -\pi/4$. For the bulk of the simulations reported herein, the amplitude $\Omega_0$ of the angular velocity of the rotating arc-walls was fixed at $\Omega_0 = 150$. Occasionally, the amplitude of forcing was increased in order to explore solutions of increasing the mixing efficiency ; see Sec. 4.2.

The flow is considered incompressible and governed by the Navier-Stokes equation coupled to the advection-diffusion equation that describes the

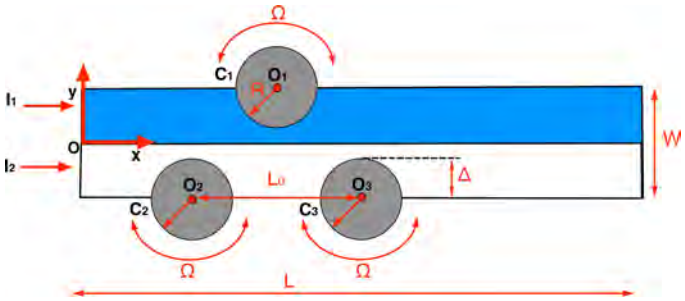


**Fig. 1** Schematic representation of the channel equipped with three rotating arc-walls (in scale).

dynamics of the passive scalar $C$ to be mixed:

$$\nabla \cdot \boldsymbol{v} = 0, \tag{4}$$

$$\rho \partial_t \boldsymbol{v} + \rho(\boldsymbol{v} \cdot \nabla)\boldsymbol{v} = -\nabla p + \nabla \cdot \left[2\eta\left(\dot{\gamma}\right)\boldsymbol{D}\left(\boldsymbol{v}\right)\right], \tag{5}$$

$$\partial_t C = \mathcal{D}\nabla^2 C - \boldsymbol{v} \cdot \nabla C. \tag{6}$$

Here, $\boldsymbol{v} = (v_x, v_y)$, $\rho$, $t$, $p$ represent velocity, density, time and pressure; $\boldsymbol{D}(\boldsymbol{v}) = \frac{1}{2}\left[(\nabla \boldsymbol{v}) + (\nabla \boldsymbol{v})^T\right]$ is the rate deformation tensor, $\dot{\gamma}$ its second invariant, $\eta\left(\dot{\gamma}\right)$ is the effective viscosity, and $\mathcal{D}$ is the molecular diffusivity of the passive scalar $C$.

A regularized Herschel-Bulkley constitutive relationship is used, following [Papanastasiou(1987)]:

$$\eta\left(\dot{\gamma}\right) = K_0 \dot{\gamma}^{N-1} + \tau_y \frac{1 - \mathrm{e}^{-m\dot{\gamma}}}{\dot{\gamma}}, \tag{7}$$

where $K_0$ stands for the consistency, $\tau_y$ for the yield stress, $N$ for the power law index and $m$ for the regularisation parameter. For all the numerical simulations reported herein, the regularisation parameter was maintained constant at $m = 1200$, and the consistency was $K_0 = 1$.

The governing equations (4)-(6) above are supplemented by no-slip boundary conditions at the static and moving walls. Through the inlets $I_{1,2}$ of the flow channel, two identical fluid streams to be mixed are evenly injected at a constant bulk velocity $U_0$. For all simulations reported herein, the bulk velocity is fixed at $U_0 = 2$. At the initial time $t_0 = 0$, the interface between the two fluid streams is placed at the position $y = 0$ (see Fig. 1).

To define the non-dimensional groups governing the viscoplastic flow and the mixing problem, we follow [Thompson and Soares(2016)]. With the bulk velocity $U_0$ as reference velocity and the width channel $W$ as reference length

(see Fig. 1), a bulk Reynolds number is defined as

$$\mathrm{Re}_{\mathrm{bulk}} = \frac{\rho U_0^2}{\tau_y + K_0 \left(\frac{2U_0}{W}\right)^N}. \tag{8}$$

By varying the rheological properties of the fluids (mainly the yield stress $\tau_y$) while maintaining a constant bulk velocity $U_0$, the bulk Reynolds number $\mathrm{Re}_{\mathrm{bulk}}$ was varied in the interval $[0.0514, 1]$. The bulk Bingham number, which quantifies the balance between the yield stress and viscous stress in the mean flow is defined as

$$\mathrm{Bn}_{\mathrm{bulk}} = \frac{\tau_y}{K_0 \left(\frac{2U_0}{W}\right)^N}. \tag{9}$$

By varying the yield stress $\tau_y$ and maintaining a constant power law index at $N = 0.75$, the bulk Bingham number was varied in the range $\mathrm{Bn}_{\mathrm{bulk}} \in [0, 26.5]$.

The competition between advection and diffusion during the mixing process is quantified by the bulk Péclet number defined as

$$\mathrm{Pe}_{\mathrm{bulk}} = \frac{U_0 W}{\mathcal{D}}. \tag{10}$$

where $\mathcal{D}$ is the molecular diffusion coefficient of the passive scalar. The Péclet number was fixed at $\mathrm{Pe}_{\mathrm{bulk}} = 2 \times 10^6$ for all the cases we have studied. This is indeed a large value and the technical ability of reaching it in a reliable manner will be detailed in Sec. 2.3.

Next, by introducing a velocity scale related to the external forcing generated by the rotating arc-walls denoted by $U_f = R\Omega_0$, a Reynolds number associated to the strength of the external forcing may be defined in a similar manner as the bulk Reynolds number $\mathrm{Re}_{\mathrm{bulk}}$ as

$$\mathrm{Re}_f = \frac{\rho U_f^2}{\tau_y + K_0 \left(\frac{2U_f}{W}\right)^N}. \tag{11}$$

The ratio

$$K = \frac{U_f}{U_0} \tag{12}$$

represents the strength of the external forcing relative to the mean flow velocity, and may be understood as a quantitative measure of the energy injected into the hydrodynamic system in order to achieve efficient mixing. The largest value of the Reynolds number associated to the external forcing was $\mathrm{Re}_f^{\max} = 26.8$, meaning that the forcing might introduce some mild inertial effects particularly in the vicinity of the rotating arc-walls.

As the characteristic rates of shear are typically larger within the *"active"* mixing region located in between the rotating arc-walls, a Bingham number

related to the external forcing is defined as

$$\mathrm{Bn}_f = \frac{\tau_y}{K_0 \left(\frac{2U_f}{W}\right)^N}. \tag{13}$$

This Bingham number is clearly smaller than the bulk Bingham number ($\mathrm{Bn}_f < \mathrm{Bn}_{\mathrm{bulk}}$), indicating that one expects within the *"active"* mixing regions to find un-yielded material blobs with sizes smaller than that of the central un-yielded plug observed at the outlet of the mixer. The forcing Bingham number was varied in the range $\mathrm{Bn}_f \in [0, 2.24]$. For simplicity, we chose to index the various data sets discussed through the paper in terms of the bulk Bingham number $\mathrm{Bn}_{\mathrm{bulk}}$.

Of particular relevance to this study is the bulk Strouhal number that relates the characteristic time scale of the main flow to that of the external forcing:

$$\mathrm{St}_{\mathrm{bulk}} = \frac{W}{TU_0}. \tag{14}$$

Here, $T$ stands for the period of rotation of the arc-walls, $T = 2\pi/f$ with $f$ the frequency. For all the simulations described herein, $T = 0.5$. Consequently, the Strouhal number was fixed through all the simulations reported herein, $\mathrm{St}_{\mathrm{bulk}} = 1$. Also, the forcing ratio was fixed at $K = 27$.

Based on both the theoretical arguments and the numerical simulation results presented in Ref. [El Omari et al(2021)El Omari, Younes, Burghelea, Castelain, Moguen, and Le Guer], this choice of non-dimensional numbers is consistent with an efficient mixing for the Newtonian case to which we will systematically refer to as the *"reference"* case. However, we note here that neither the stirring protocol nor the geometry of the mixer were identical to those illustrated in Ref. [El Omari et al(2021)El Omari, Younes, Burghelea, Castelain, Moguen, and Le Guer]. Yet, the phenomenological conditions for efficient mixing derived in Ref. [El Omari et al(2021)El Omari, Younes, Burghelea, Castelain, Moguen, and Le Guer] in terms of $\mathrm{Pe}_{\mathrm{bulk}}$, $\mathrm{St}_{\mathrm{bulk}}$ and $K$ remain valid as they are rather general and independent on the exact details of the stirring protocol and exact geometrical dimensions of the stirring elements.

## 2.2 Numerical method

To solve numerically the flow problem described in Section 2.1, we use the open source flow solver Gerris which was presented in Refs. [Popinet(2003), Popinet(2009), Popinet(2015)]. The $2D$ domain is discretized using square finite volumes organised hierarchically as a quad-tree, which allows for dynamical local grid adaptation (refinement or coarsening). This feature is highly suitable in order to properly capture the stretching and folding experienced by the fluid due to the cylinder rotations, as well as to highlight the role of the diffusion and the dynamic of the solid material elements. Three refinement criteria are used for the grid adaptation: a criterion based on the local value of the

vorticity, a criterion based on the local gradient of the concentration $C$, and a criterion allowing to refine near the solid zones. A cell of the grid is refined whenever at least one of the three criteria is satisfied. The variables $\boldsymbol{v}$, $p$ and $C$ are co-located at the centre of each finite volume. Their values at the computational cell centre are interpreted as surface-average values for this discretization cell. The pressure is obtained by means of a multilevel Poisson solver, where the multilevel hierarchy of the quad-tree is used to accelerate the resolution by multigrid V-cycling. The code uses a second order accurate staggered-in-time discretization, combined by fractional-step projection method that satisfies the incompressibility constraint at the end of each time step. A conservative formulation is used to evaluate the advection term of eqs. (5) and (6) which are solved with a second-order upwind numerical scheme. The viscous terms are treated implicitly with a Crank-Nicolson scheme. The time step is dynamically adapted to satisfy the CFL condition CFL $\leq 0.75$ within each computational cell. The overall code (Gerris) is second-order accurate in both space and time.

The presence of solid boundaries (duct walls and rotating cylinders) if treated by volume-of-fluid approach. At these wall boundaries, a Dirichlet-type condition is applied for the velocity, and a Neumann condition is applied for the transport of the tracer concentration i.e. $\partial_n C = 0$ ($n$ being the wall normal direction). A similar boundary condition is applied for the pressure. At the inlet, Dirichlet boundary conditions are used for the velocity and the tracer, with prescribed values, and Neumann boundary condition is applied to the pressure ($\partial_n p = 0$). The prescribed values or profiles are given in the previous Section. At the outlet, a prescribed value was applied for pressure $p = 0$, and Neumann boundary condition is applied for the other variables: $\partial_n(\boldsymbol{v}, C) = 0$.

## 2.3 Diffusion length and mesh size

Through this study, we are interested in the high Péclet number limit where the mixing is primarily driven by laminar chaotic advection rather than by the molecular diffusion. Such case is rather difficult to properly capture in numerical simulations as it implicitly requires very fine meshing in the vicinity of the passive scalar interfaces. A characteristic length relevant to the degree of fineness of the spatial discretization near the interface is the diffusion length $l_{\text{diff}}$ defined with the characteristic advection time $t_{\text{adv}} = L/U_{\max}$ for a fluid particle to cross the mixing zone,

$$l_{\text{diff}} = 2\sqrt{\mathcal{D}t_{\text{adv}}} = 2\sqrt{\frac{\mathcal{D}L}{U_{\max}}}. \tag{15}$$

Here, $U_{\max}$ stands for the maximal velocity across the width of the channel at the outlet which, in the viscoplastic cases, corresponds to the speed of the solid plug [1].

[1] Note that, as the flow develops downstream, $U_{\max}$ is generally larger than the inlet speed $U_0$ but, of course, of the same order of magnitude.

We obtain the non-dimensional diffusion length the value $l_{\text{diff}} = 3.16 \times 10^{-3}$, and the requirement for a characteristic mesh size to be smaller than $l_{\text{diff}}$ leads to a total number of grid elements for the entire domain of the order of 1 035 000. We consider such a fine grid too costly for the large number of simulations needed for comparison to the results obtained from the conditions. The analytical solution for the transverse profile of the passive scalar distribution at the end of the mixer is given by:

$$C(y) = \left[1 + \text{Erf}\left(\frac{y}{\sigma}\right)\right] \frac{1}{2} \tag{16}$$

Here $\text{Erf}(\cdot)$ stands for the error function and the dispersion coefficient $\sigma$ is related to the *"effective"* diffusion coefficient $\mathcal{D}_{\text{eff}}$, $\sigma = 2\sqrt{\frac{\mathcal{D}_{\text{eff}} x}{U_0}}$. By the *"effective"* diffusion coefficient we understand here a value that encompasses both the molecular diffusive effects and the artificial diffusive effects inherently introduced by limited mesh size in the vicinity of the passive scalar interface.

If the mesh size is sufficiently small in the vicinity of the passive scalar interface then the effective diffusion coefficient obtained by fitting the transverse profiles of the concentration according to Eq. 16 should be comparable in magnitude to the molecular diffusion coefficient, i.e. $\frac{\mathcal{D}_{\text{eff}}}{\mathcal{D}} \approx 1$. The comparative results of the transverse profiles of the passive scalar concentration obtained for various levels of mesh refinement using non-adaptive meshing and adaptive meshing are summarised in Fig. 2(a). For the cases of regular grids, the mesh size is constant and related to the level of refinement, $\Delta y = W/2^{\text{LEVEL}}$. The full lines in each panel of Fig. 2(a) are nonlinear fitting functions according to the analytical solution for the transverse distribution of the passive scalar, Eq. 16. The first three panels from the top present the results obtained for a regular (non adaptive) grid with various sizes $\Delta y_{\text{min}}$ decreasing from the top to the bottom. The dependence of the effective diffusion coefficient obtained by fitting each concentration profile illustrated in Fig. 2(a) by the analytical solution defined by Eq. 6 on the minimal mesh size $\Delta y_{\text{min}}$ is shown in Fig. 2(b).

It is rather clear from the mesh study summarized in Fig. 2 that the only level of refinement of the regular grid able to resolve the interface of the passive scalar is 8 (which gives $\Delta y_{\text{min}} = 0.0039$). Such fine mesh is, however, very expensive from a computational standpoint and, consequently, unpractical. This difficulty may be circumvented by resorting to adaptive meshing instead of a regular one which is a unique feature of the Gerris flow solver, [Popinet(2003)]. Three distinct types of grid adaptivity are simultaneously employed through this study. First, for the reasons detailed above, we use adaptive meshing in the vicinity of the passive scalar interface. Second, as the external forcing of the flow locally generates strong vorticity, we adapt the mesh based on the the local magnitude of the vorticity. This is important for properly resolving the flow kinematics (particularly the dynamics around the hyperbolic and elliptical points) which is of key relevance to understanding

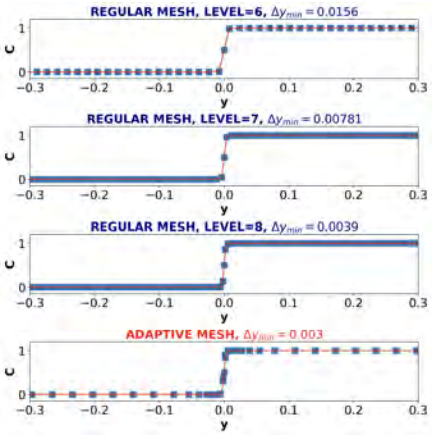


(a)

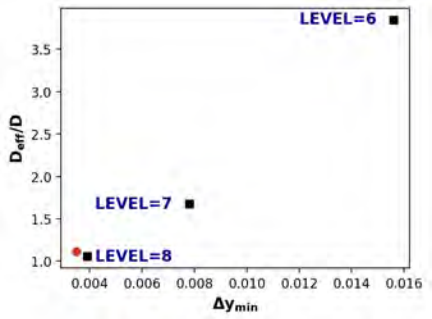


(b)

**Fig. 2** (a) Transverse profiles of the passive scalar concentration $C$ at the exit of the mixer obtained for various values of the smallest mesh size $\Delta y_{\min}$ indicated in the top inserts. The case illustrated in the bottom panel refers to the adaptive meshing technique - see text for description. The full lines in each panel are nonlinear fitting functions according to the analytical solution (see text for the description/discussion). (b) Dependence of the effective diffusion coefficient normalised by the molecular diffusion coefficient $\frac{\mathcal{D}_{\text{eff}}}{\mathcal{D}}$ on the mesh size in the vicinity of the passive scalar interface, $\Delta y_{\min}$ computed for regular mesh (black squares) obtained from the data sets presented in the top three sub-panels of Fig. 2(a) and the adaptive mesh (red circle) obtained from the data set presented in the bottom panel of Fig. 2(a).

the dynamics of mixing process. Third, as we aim to understand the dynamics of the mixing process in relation to the viscoplastic nature of the fluids, we need to properly identify the yield surfaces at each time instant and ultimately the characteristic sizes of the un-yielded material elements. For this purpose, an extra mesh adaptivity controlled by the local value of the viscosity was employed.

The adaptive grid obtained by combining all three criteria stated above is illustrated in Fig. 3. We have purposely chosen for illustration the highest yield stress case investigated ($\text{Bn}_{\text{bulk}} = 26.5$) and a mild shear thinning ($N = 0.75$)

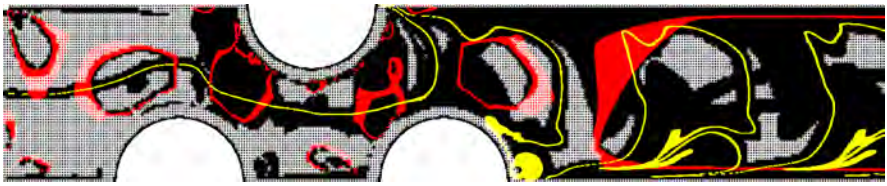

**Fig. 3** Illustration of the adaptive grid during a simulation of the mixing process at large bulk Bingham number, $\mathrm{Bn}_{\mathrm{bulk}} = 26.5$. The dense grid points coloured in yellow mark the interface of the passive scalar while those marked in red mark the yield surface (see text for description). The dense black grid points have resulted from the vorticity based dynamic mesh adaptivity.

in order to exemplify the identification of the yield surfaces. The grid points coloured in yellow mark the interface of the passive scalar while those coloured in red the yield surface.

For all the numerical results reported herein the same adaptive meshing has been used.

# 3 Results

## 3.1 Role of yield stress on the space-time dynamics of the mixing process

Prior to studying the coupling between the yield stress behavior and the mixing process, we briefly discuss in the following a reference case where both fluids are Newtonian ($\mathrm{Bn}_{\mathrm{bulk}} = 0$, $N = 1$). Both the in-flow conditions ($\mathrm{Re}_{\mathrm{bulk}}$, $\mathrm{Pe}_{\mathrm{bulk}}$) and the external forcing conditions ($\mathrm{St}_{\mathrm{bulk}}$, $K$) are purposely chosen (using both the theoretical predictions and numerical results presented in Ref. [El Omari et al(2021)El Omari, Younes, Burghelea, Castelain, Moguen, and Le Guer]) such that efficient mixing is observed at the outlet of the mixer. Spatial distributions of the passive scalar concentration $C$ obtained for the reference Newtonian case at several time instants scaled by the period of the forcing are illustrated in Fig. 4.

As already stated, this test case was purposely chosen to obtain efficient mixing. Consequently, a rather homogeneous mixture is obtained after roughly ten periods of rotation of the arc-walls. To assess the space-time dynamics of the mixing process it is convenient to build space-time diagrams by recording the profile of the concentration along a fixed line orthogonal to the mean flow direction $x$. We illustrate in Fig. 5(a) space-time diagrams built for the Newtonian case at the centre of the mixer (*i.e.* at an axial position corresponding to the centre of the top rotating arc-wall) - top panel and at the exit of the mixer - bottom panel. Using the space-time diagrams one can define a mixing indicator in the form of a time series of the variance of the passive scalar distribution along the spatial coordinate,

$$C_{\mathrm{std}}(t) = \left\langle \left(C(y,t) - C_{\mathrm{av}}(t)\right)^2 \right\rangle_y^{0.5} \tag{17}$$

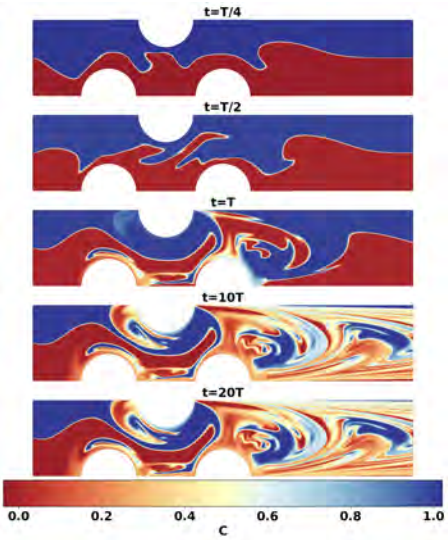


**Fig. 4** Mixing patterns for the Newtonian case ($\mathrm{Bn}_{\mathrm{bulk}} = 0$, $N = 1$) at several time instants indicated in the top inserts.

with $C_{\mathrm{av}}(t) = \langle C(y,t)\rangle_y$ and $\langle\cdot\rangle_y$ denoting the average along the $y$ direction. Time series of the mixing indicator $C_{\mathrm{std}}$ obtained for the Newtonian case at the centre (the circle) and at the exit of the mixer (the square) are illustrated in Fig. 5(b). Regardless the axial position of observation, the mixing indicator $C_{\mathrm{std}}$ oscillates around a steady state value with a periodicity set by the periodicity of the external forcing, $T$. Two important details distinguish the passive scalar evolution within the central part from that observed at its exit. First, the steady state value $C_{\mathrm{std}}^{\mathrm{av}}$ of the fluctuations of the $C_{\mathrm{std}}$ is clearly smaller at the exit of the mixer than at its centre which indicates a progressively better mixing as the two fluids advance downstream. Second but equally relevant from a practical perspective, the magnitude of the fluctuations of the mixing indicator around its steady state value $\delta C_{\mathrm{std}}$ which, bearing in mind the Taylor's frozen flow hypothesis, may be interpreted as a crude (but yet meaningful) measure of the homogeneity of the mixing process: at the centre of the mixer the mixing is very in-homogeneous whereas a significantly more homogeneous mixing is observed at the exit of the mixer. The characteristic time scale $t_d$ associated to the mixing process may be estimated by noting that the mixing indicator $C_{\mathrm{std}}$ depends exponentially on time, $C_{\mathrm{std}}(t) = C_{\mathrm{std}}^{\mathrm{av}} + A\mathrm{e}^{\frac{t-t_a}{t_d}}$ - the full line in Fig. 5(b). Such an exponential decay of the passive scalar variance is a hallmark of the so called *"Batchelor regime of mixing"* realised in temporally random and spatially smooth flows, [Batchelor(1959), Kraichnan(1968)].

Of particular relevance in understanding the topology of the mixing patterns is the analysis of the mixing boundary layers. Indeed, after a close inspection of the space time diagram acquired at the exit of the mixer (bottom

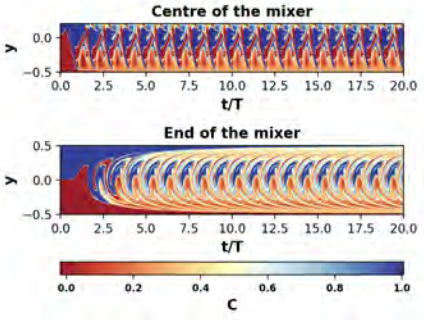


(a)

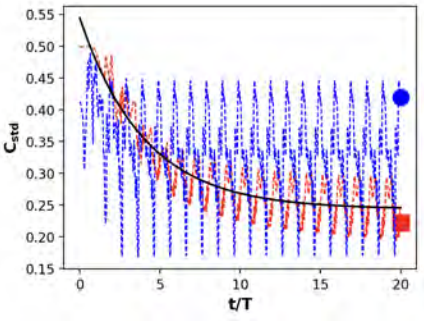


(b)

**Fig. 5** (a) Space time plots obtained for the Newtonian case ($Bn_{bulk} = 0$, $N = 1$) at the centre of the mixer (top panel) and at the exit of the mixer (bottom panel). (b) Time series of the mixing indicator $C_{std}$ obtained for the Newtonian case ($Bn_{bulk} = 0$, $N = 1$) at the centre of the mixer (circle) and at the exit of the mixer (square). The full line is an exponential fitting function.

panel in Fig. 5(a)) one notes that within narrow regions located in the proximity of the top/bottom boundaries of the channel no mixing occurs: within these regions called mixing boundary layers the passive scalar gets trapped and the effects of the periodic forcing are no longer felt. To identify the mixing boundary layers we focus on the dependence of the power of the concentration fluctuations defined as $P_f$ on the transverse coordinate $y$. Corresponding to each value of the vertical coordinate $y = y_0$ the power $P_f$ of the fluctuations is obtained by computing the Fourier power spectrum of the time series $C(t)|_{y=y_0}$ and averaging it over the entire frequency domain.

The analysis of the mixing boundary layer for the Newtonian case is summarised in Fig. 6. The transverse profile of the power of the fluctuations of the passive scalar fluctuations $P_f(y)$ computed over the last five periods of the mixing process (see the space-time plot in panel **(a)** of Fig. 6) are illustrated in panel **(b)** of Fig. 6). The edges of the top and bottom mixing boundary layers may be identified by the positions where the power of fluctuations starts to increase significantly. The flow region characterised by large values of $P_f$

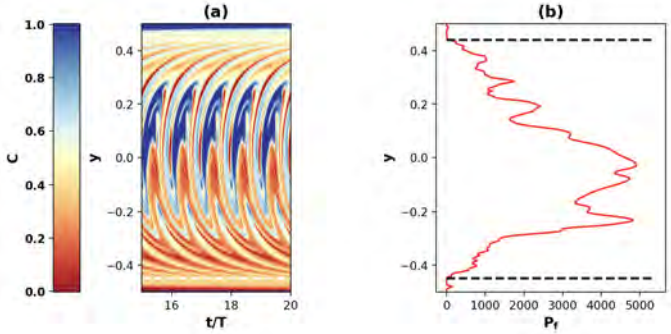


**Fig. 6** Illustration of the mixing boundary layer for the Newtonian case ($\mathrm{Bn}_{\mathrm{bulk}} = 0$, $N = 1$): **(a)** Space time diagram of the passive scalar distribution during the last 5 periods of the mixing. **(b)** Transverse profile of the average spectral power of the fluctuations of the passive scalar $P_f$. In both panels the horizontal dotted lines mark the edges of the top and bottom mixing boundary layers.

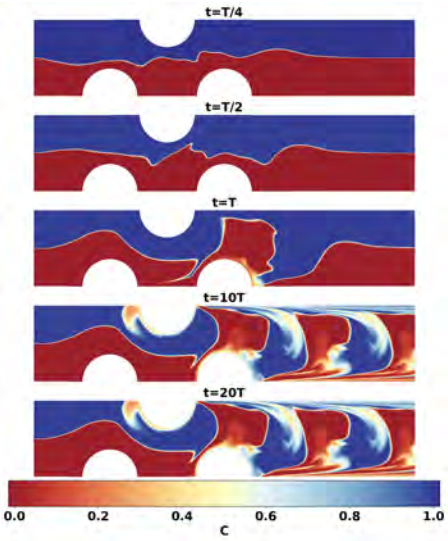


**Fig. 7** Mixing patterns for largest yield stress explored ($\mathrm{Bn}_{\mathrm{bulk}} = 26.5$, $N = 0.75$) at several time instants indicated in the top inserts.

will be further referred to as the *bulk* of the flow. Within the mixing of the boundary layers the magnitude of the passive scalar fluctuations is significantly smaller than in the bulk of the flow, Fig. 6**(b)**.

We now turn our attention to the mixing in the presence of yield stress ($\mathrm{Bn}_{\mathrm{bulk}} = 26.5$) and a mild shear thinning behavior ($N = 0.75$).

The distributions of the passive scalar computed at several time instants are illustrated in Fig. 7. In this case, the mixing is very poor and limited to narrow regions locating in the close vicinity of the rotating arc-walls. The spatial distributions of the passive scalar consist of a periodic alternation of

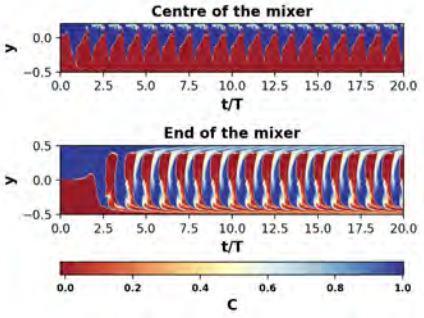


(a)

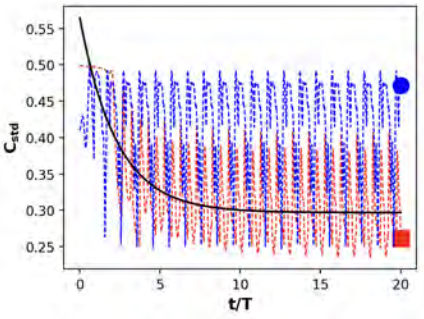


(b)

**Fig. 8** (a) Space time plots of the passive scalar $C$ obtained for the highest yield stress case ($\mathrm{Bn}_{\mathrm{bulk}} = 26.5$, $N = 0.75$) at the centre of the mixer (top panel) and at the exit of the mixer (bottom panel). (b) Time series of the mixing indicator $C_{\mathrm{std}}$ obtained for the highest yield stress case ($\mathrm{Bn}_{\mathrm{bulk}} = 26.5$, $N = 0.75$) at the centre of the mixer (circle) and at the exit of the mixer (square). The full line illustrates a failed attempt to fit exponentially the time series of the mixing indicator at the channel exit.

un-mixed fluid patches along the mean flow direction. The relevant space scales associated to this passive scalar space distribution are mainly set by the mean flow speed and the time scale at each the external forcing is imposed, $T$. The dramatic effect of the yield stress on the mixing efficiency becomes even clearer if one plots space-time diagrams, Fig. 8(a). At the centre of the mixer a saw tooth space-time pattern is observed - top panel in Fig. 8(a). This is most probably due to the presence of un-yielded material units within the central zone of the mixer which prevent the formation of the hyperbolic flow region that promotes mixing. The relationship between the yielded/un-yielded zones and the flow kinematics will be explored in more detail in Secs. 3.2 and 3.3.

At the exit of the mixer the space-time plot reveals a time periodic alternation of the two fluids with some very weak mixing that may be observed in the proximity of the channel boundaries - bottom panel in Fig. 8(a).

Consequently, the time series of the mixing indicator $C_{\mathrm{std}}$ reveals both a poor level of mixing reflected by the large value of steady state value $C_{\mathrm{std}}^{\mathrm{av}}$

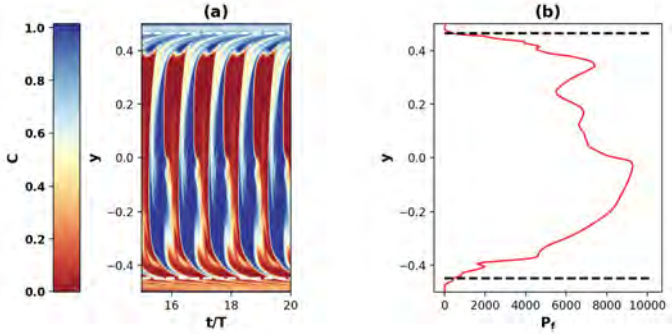


**Fig. 9** Illustration of the mixing boundary layer for the largest yield stress case ($\mathrm{Bn}_{\mathrm{bulk}} = 26.5$, $N = 0.75$) **(a)** Space time diagram of the passive scalar distribution during the last 5 periods of the mixing **(b)** Transverse profile of the average spectral power of the fluctuations of the passive scalar $P_f$. In both panels the horizontal dotted lines mark the edges of the top and bottom mixing boundary layers.

and a strongly in-homogeneous evolution of the passive scalar reflected by the large variance $\delta C_{\mathrm{std}}$. Unlike in the Newtonian case, the time series of the concentration variance can no longer be well fitted by an exponential decay function which is another indicator that the yield stress behavior prevents the efficient stretching and folding of material elements responsible for the time-exponential decay of the passive scalar in a temporally random and spatially smooth flow. We may conclude this part by noting that the loss of mixing efficiency is dramatic for this large value of the Bingham number, $\mathrm{Bn}_{\mathrm{bulk}} = 26.5$, and in the presence of a mild shear thinning, $N = 0.75$.

As compared to the Newtonian case illustrated in Fig. 6, the boundary layers observed in the presence of yield stress are thinner, Fig. 9. Also and equally interesting is that in this case the transverse profile of the power $P_f$ of the passive scalar fluctuations exhibits fewer local peaks - panel (b) in Fig. 9. This indicates that the passive scalar decay (manifested through the local power of fluctuations) is carried on in this case within a narrower range of space scales. This remark corroborates well with the loss of mixing efficiency we observe at high Bingham numbers.

To summarize the analysis of the mixing boundary layers we present in Fig. 10 the dependence of the width of the top and bottom layers on the Bingham number $\mathrm{Bn}_{\mathrm{bulk}}$. As the Bingham number is gradually increased, the width of both the top and bottom boundary layers decreases.

To understand the impact that a gradual increase of the bulk Bingham number has on the mixing efficiency we present in Fig. 11 space-time plots constructed at the exit of the mixer similar to those illustrated in the bottom panels of Figs. 5(a), 8(a) for various Bingham numbers indicated in the top inserts. For all cases the power law index is fixed $N = 0.75$ except for the Newtonian case (the top panel) where $N = 1$.

For all data sets illustrated in Fig. 11 the flow conditions ($\mathrm{Pe}_{\mathrm{bulk}}$, inflow speed $U_0$) and forcing conditions ($\mathrm{St}_{\mathrm{bulk}}$, $K$) are identical. Due to the gradual

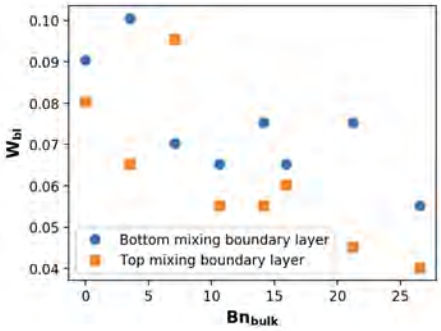


**Fig. 10** Dependence of the width of the top and bottom mixing boundary layers on the Bingham number $\mathrm{Bn}_{\mathrm{bulk}}$.

increase of the yield stress both the bulk Reynolds number $\mathrm{Re}_{\mathrm{bulk}}$ and the Reynolds number associated to the forcing $\mathrm{Re}_f$ decrease gradually.

As the bulk Bingham number increases (from the top to the bottom) a gradual change in both the space and time scales of the passive scalar distributions marking the gradual transition from good mixing to critically poor one is observed.

To sum up the discussion on the role of the Bingham number on the mixing efficiency and its homogeneity we present in Fig. 12 the dependence of the steady state value $C^{\mathrm{av}}_{\mathrm{std}}$ of the time series of the variance of the concentration for all the cases investigated. Both the colours and the sizes of the symbols in Fig. 12 related to the degree of homogeneity of the mixture indicated by $\delta C_{\mathrm{std}}$. It is rather clear that for fixed flow conditions (inflow speed $U_0$, bulk Péclet number $\mathrm{Pe}_{\mathrm{bulk}}$, bulk Strouhal number $\mathrm{St}_{\mathrm{bulk}}$ and forcing amplitude $K$) the mixing efficiency decreases abruptly starting from a critical Bingham number $\mathrm{Bn}^c_{\mathrm{bulk}} \approx 5$. Beyond this onset, both the mixing efficiency and the degree of homogeneity of the mixture remain roughly unchanged but, from a practical standpoint, are clearly unsatisfactory.

Quite interestingly on the other hand is that for $\mathrm{Bn}_{\mathrm{bulk}} = 3.5$ the mixing efficiency is practically identical to that obtained for the Newtonian case. This fact may be due to the presence of shear thinning ($N = 0.75$).

The non-monotonic variation of the mixing efficiency with the bulk Bingham number observed for $\mathrm{Bn}_{bulk} > \mathrm{Bn}^c_{\mathrm{bulk}}$ in Fig. 12 is counter-intuitive and needs a separate discussion. The evolution of the passive scalar within the boundary of the flow is significantly different from that in the bulk. Below the critical Bingham number $\mathrm{Bn}_c \approx 5$ a good mixing is observed in the bulk of the flow, Fig. 6(a). On another hand, the behavior in the boundary layer is quite different. A careful inspection of the same figure reveals rather poor mixing (the top and bottom parts of the space-time diagram) in the vicinity of the channel's walls in the form of layers of un-mixed fluids. As the Bingham number is increased past the critical Bingham number $\mathrm{Bn}_c$, un-mixed fluid regions appear in the bulk of the flow as well, Fig. 9(a). These un-mixed

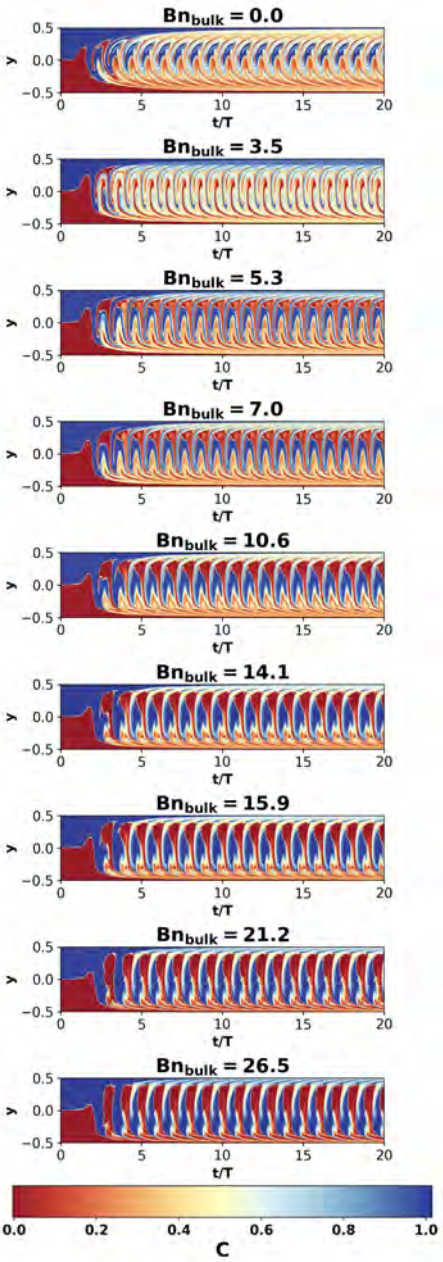


**Fig. 11** Panorama of the space-time diagrams of the passive scalar $C$ at the exit of the mixer obtained for several bulk Bingham numbers $\mathrm{Bn_{bulk}}$ indicated in the top inserts.

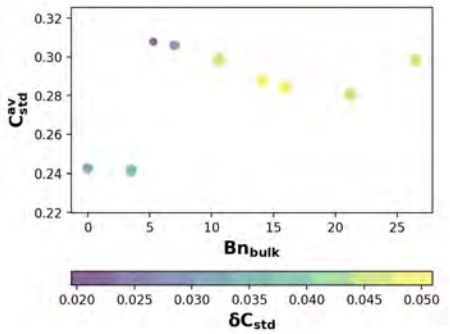


**Fig. 12** Dependence of the mixing efficiency defined as the variance of the passive scalar concentration at the exit of the mixer, $C_{\mathrm{std}}$, on the bulk Bingham number $\mathrm{Bn}_{\mathrm{bulk}}$. Both the color and the relative size of the symbols map the fluctuations $\delta C_{\mathrm{std}}$ of the mixing indicator $C_{\mathrm{std}}$ around its dynamical steady state value.

regions are very different from the un-mixed regions observed near the boundaries as they are due to the appearance of solid (unyielded) material blobs that travel downstream. While by the way we have defined the mixing indicator $C^{av}_{std}$ it is clear that both the bulk and boundary layer behaviors contribute to the overall mixing efficiency, these two contributions evolve differently when the Bingham number is gradually increased. Thus, for $\mathrm{Bn} \geq \mathrm{Bn}_c$, two phenomena with opposite tendencies are observed. First, the width of the un-mixed (homogeneous) boundary layers decreases monotonically with $\mathrm{Bn}_{bulk}$, Fig. 10. This leads to a temporary decrease of $C^{av}_{\mathrm{std}}(t)$ or, in other words, an apparent increase in the overall mixing efficiency observed in Fig. 12 in the range $\mathrm{Bn}_{bulk} \in [5, 15]$. Simultaneously with this, un-yielded blobs are equally present in the bulk of the flow. As it will be demonstrated later through paper (in connection to the upcoming Fig. 22), the average size of these un-yielded blobs increases monotonically with $\mathrm{Bn}_{bulk}$. For $\mathrm{Bn}_{bulk} \geq 15$ the contribution of the boundary layers to the overall mixing efficiency is overcome by the bulk behavior simply because in this range of Bingham numbers the overall width of the boundary layers becomes systematically smaller than the average size of the un-yielded which finally explains the up-turn of the mixing efficiency observed around $\mathrm{Bn}_{bulk} \approx 15$ in Fig. 12.

## 3.2 Role of the yield stress on the space-time dynamics of the flow fields: an Eulerian description

On an intuitive basis, one expects that the dramatic loss of mixing efficiency observed while the bulk Bingham number is gradually increased past a critical value $\mathrm{Bn}^c_{\mathrm{bulk}} \approx 5$ originates from dramatic changes of the space-time dynamics of the flow fields triggered by the presence of the yield stress. It therefore appears natural to systematically describe the flow structure in an Eulerian frame of reference at various bulk Bingham numbers and attempt to correlate

the findings/conclusions with the space-dynamics of the passive scalar detailed in Sec. 3.1. To this we dedicate the present section.

### 3.2.1 Flow structure

We focus first on the time averaged profiles of each velocity component observed at the outlet of channel, Fig. 13. The numerical data are averaged during the last five periods of the mixing process, $15T \leq t \leq 20T$.

In all cases we have studied the magnitude of the axial component, Fig. 13(a), is significantly larger than that of the transverse velocity, Fig. 13(b). This means that, in all the cases we study, the mixing is mainly carried on within the central part of the mixer (the *"active"* mixing zone located in between the rotating arc-walls) while towards its outlet the mixing can be slightly improved solely by the molecular diffusion which, due to the high value of the Péclet, is not very effective. For the Newtonian reference case ($\mathrm{Bn}_{\mathrm{bulk}} = 0, N = 1$) the transverse profile is nearly parabolic (note that, due to the presence of the external forcing, at the exit of the channel the transverse component $v_y$ of the velocity is not zero). As the bulk Bingham number is gradually increased a central plug in the transverse profile of the axial velocity develops, Fig. 13(a). It is equally instructive to note that for $\mathrm{Bn}_{\mathrm{bulk}} > 0$ no fluctuations of the axial velocity (highlighted by the shaded regions) may be observed meaning that while advancing downstream past the *"active"* mixing the flow patterns are practically *"frozen"*.

The dependence of the widths of the yielded zones observed in the proximity of the walls (or the viscoplastic boundary layers) at the outlet of the mixing channel on the bulk Bingham number $\mathrm{Bn}_{\mathrm{bulk}}$ is presented in Fig. 13(c). For low values of the bulk Bingham number a slight asymmetry of the top/bottom viscoplastic boundary layers due to the asymmetry of the external forcing (we have two rotating arc-walls on one side of the channel and only one on the opposite side) is observed. At large bulk Bingham numbers, however, this asymmetry vanishes indicating once more that at the channel outlet the flow patterns are *"frozen"* and the effect of the forcing is no longer felt. The width of the viscoplastic boundary layers decays algebraically with the bulk Bingham number, $W_{\mathrm{vpbl}} \propto \mathrm{Bn}_{\mathrm{bulk}}^{-0.39 \pm 0.015}$ - the full line in Fig. 13(c). This scaling relationship is rather close to the one proposed by Piau and Debiane $W_{\mathrm{vpbl}} \propto \mathrm{Bn}_{\mathrm{bulk}}^{-\frac{N}{N+1}} = \mathrm{Bn}_{\mathrm{bulk}}^{-0.428}$, [Piau and Debiane(2004)].

It is interesting at this point to compare the width of the top/bottom viscoplastic boundary layers to those of the mixing boundary layers illustrated in Fig. 10 and discussed in Sec. 3.1. We note that, regardless the value of the bulk Bingham number, the width of the viscoplastic boundary layer is roughly twice larger than that of the mixing boundary layers. This indicates that, whereas in the Newtonian case the boundary layers for the passive scalar are controlled by the magnitude of the bulk Péclet number, in the viscoplastic case they are controlled by the bulk Bingham number, $\mathrm{Bn}_{\mathrm{bulk}}$.

We now turn our attention to the dependence of the Eulerian flow topology on the bulk Bingham number and correlate the changes in the flow

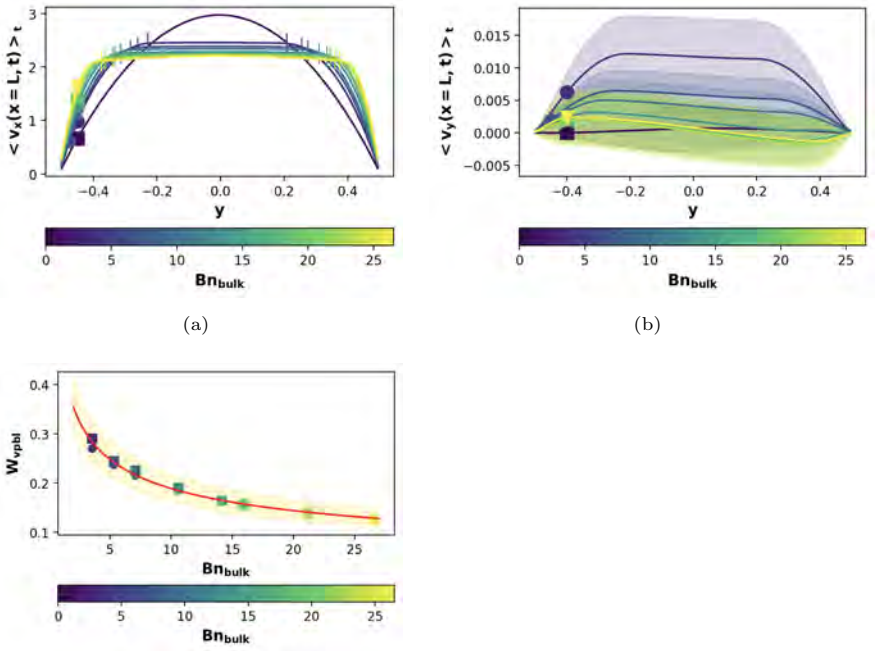


**Fig. 13** (a) Time averaged transverse profiles of the axial velocity $\langle v_x(x = L, y, t)\rangle_{15T\leq t\leq 20T}$ at the outlet of the channel. (b) Time averaged transverse profiles of the transverse velocity $\langle v_y(x = L, y, t)\rangle_{15T\leq t\leq 20T}$ at the outlet of the channel. In each panel the highlighted areas indicate the level of fluctuations of the velocity component around its mean. The vertical bars overlapped onto the curves mark the edges of the central un-yielded plug. Except for the Newtonian data set, the power law index is $N = 0.75$. The symbols refer to the value of the Bingham number: square - $\mathrm{Bn}_{\mathrm{bulk}} = 0, N = 0.75$, down triangle - $\mathrm{Bn}_{\mathrm{bulk}} = 5$, left triangle - $\mathrm{Bn}_{\mathrm{bulk}} = 3.5$, circle - $\mathrm{Bn}_{\mathrm{bulk}} = 7$, right triangle - $\mathrm{Bn}_{\mathrm{bulk}} = 10.6$, plus - $\mathrm{Bn}_{\mathrm{bulk}} = 14.1$, star - $\mathrm{Bn}_{\mathrm{bulk}} = 15.9$, pentagram - $\mathrm{Bn}_{\mathrm{bulk}} = 21.2$, hexagon - $\mathrm{Bn}_{\mathrm{bulk}} = 26.5$. (c) Dependence of the width of the yielded zones (or viscoplastic boundary layers) observed at the channel outlet on the bulk Bingham number $\mathrm{Bn}_{\mathrm{bulk}}$. The full line is a power law fitting function, $\mathrm{Bn}_{\mathrm{bulk}}^{-0.39\pm0.015}$. The shaded area highlights the confidence bounds of the power law fit. In each subplot the color map indicates the value of $\mathrm{Bn}_{\mathrm{bulk}}$.

kinematics with the evolution of the mixing efficiency as the bulk Bingham number is increased. A practically convenient way of describing the Eulerian flow topology is to illustrate the streamlines. We first illustrate in Fig. 14 streamlines computed for the Newtonian reference case at several time instants ranging in between $t = 15T$ and $t = 16T$. The rationale behind this choice is two-fold. First, as illustrated in Fig. 5(b) a dynamical steady state of the mixing is observed only for $t > 15T$. Second, as the periodic forcing induces a time periodic behavior of the flow fields it is sufficient to discuss the topology solely during a period $T$ of the external forcing. One can notice that the flow topology is different at each time instant depending on the velocity of the rotating arc-walls as well as on their sense of rotation. At each time

instant one observes elliptic points highlighted in Fig. 14 by full circles. The elliptic flow regions are formed due to the rotation of the arc-walls. Within these regions the fluid is re-circulated and one can expect that the striations of the passive scalar distributions illustrated in Fig. 4 are thus generated. As the time progresses one can notice the destruction of the re-circulating regions previously formed and the emergence of new re-circulation zones. This alternating destruction and re-formation of the elliptical regions leads to crossing of the streamlines which locally enhances the mixing process. In the vicinity of the static channel walls one can observe the formation of parabolic points highlighted by stars in Fig. 14. This is due to the non-slip boundary conditions, [Gouillart et al(2008)Gouillart, Dauchot, Dubrulle, Roux, and Thiffeault, Younes(2020), Younes et al(2022)Younes, Moguen, El Omari, Burghelea, Le Guer, and C
In panel (e) one observes a hyperbolic point highlighted by a square. The alternation of hyperbolic and elliptical flow regions is a hallmark of laminar chaotic advection and is responsible for the stretching and folding of fluid elements which ultimately translates into efficient mixing.

In order to understand the impact of the yield stress behavior on the flow topology we present in Fig. 15 streamlines computed for the largest yield stress case investigated at the same time instants illustrated for the Newtonian case. As compared to the Newtonian case, several striking differences are observed. First, the elliptical zones observed in the vicinity of the rotating arc-walls are significantly smaller in size and sometimes (e.g. in panels (b-d)) not observed at all. This can be intuitively explained by the presence of yield stress which inhibits the stretching and folding of the fluid elements. At this point one can only speculate that un-yielded material elements may exist at certain time instants within the *"active"* flow region which ultimately leads to inefficient mixing. A more systematic description of the dynamics of the solid and fluid material units will be given in Sec. 3.2.4.

One can summarise the observations described in this section by noting that the presence of the yield stress significantly alters the Eulerian topology of the flow fields mainly by inhibiting the stretching and folding of the material elements which corroborates well with the loss of the mixing efficiency observed upon a gradual increase of the bulk Bingham number $\mathrm{Bn}_{\mathrm{bulk}}$ in Sec. 3.1.

The process of chaotic advection in the flow is driven by a local alternation of shear, extension and rigid body rotation in the flow. Each of these three basic flow types is influenced by both the forcing protocol and the rheological behavior of the material. It is therefore interesting to quantify the relative contribution of each basic flow type during flows at various Bingham numbers.

The relative contributions of the shear, extension and rigid body rotation to the chaotic flow may be quantitatively assessed by the defining the non-dimensional flow parameter $\lambda$ defined implicitly via [Fuller and Leal(1981)]:

$$\nabla v = \dot{\gamma} \begin{bmatrix} 0 & 1 & 0 \\ \lambda & 0 & 0 \\ 0 & 0 & 0 \end{bmatrix} \tag{18}$$

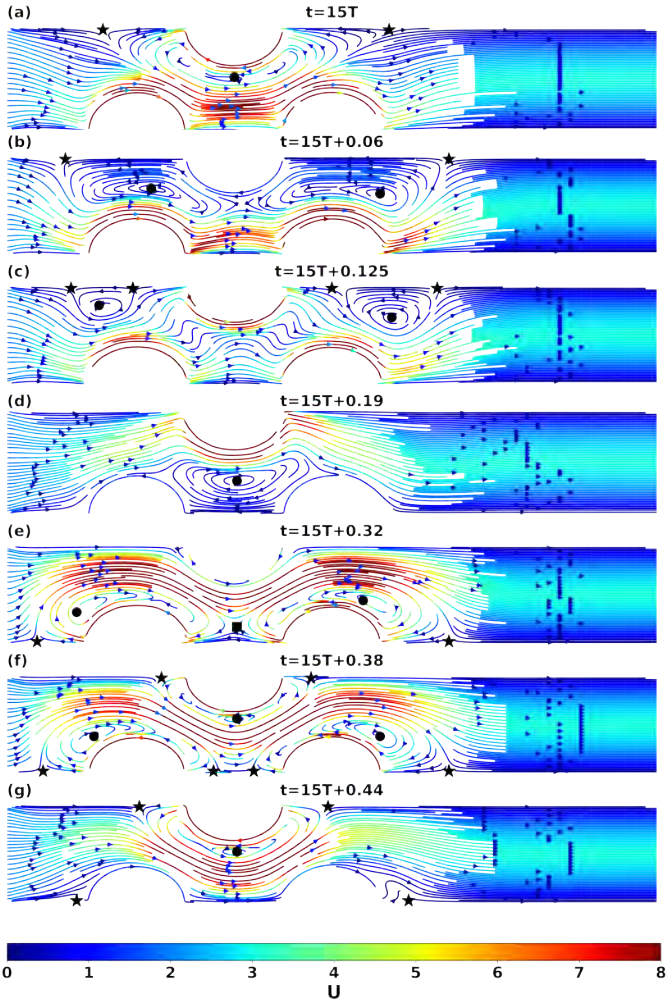


**Fig. 14** Illustration of flow topology for the Newtonian reference case at several time instants indicated in the top inserts. The colour map refers to the magnitude of the flow speed $U$. The colour bounds have been purposely chosen to highlight features within the *"active"* flow region. The symbols highlight the special points of the flow: squares- hyperbolic points, circles - elliptical points, stars - parabolic points.

Here $\dot{\gamma}$ stands for the second invariant of the rate of strain tensor and can be computed from individual velocity fields $\mathbf{U} = (u_x, u_y)$ according to:

$$\dot{\gamma} = (2\mathbf{D} : \mathbf{D})^{1/2} = \left\{ 2 \left[ \left( \frac{\partial u_x}{\partial x} \right)^2 + \frac{1}{2} \left( \frac{\partial u_x}{\partial y} + \frac{\partial u_y}{\partial x} \right)^2 + \left( \frac{\partial u_y}{\partial y} \right)^2 \right] \right\}^{1/2}. \tag{19}$$

Explicitly, the flow type parameter $\lambda$ may be written in terms of the second invariant of the rate of deformation tensor $\dot{\gamma}$ and the vorticity $\omega$:

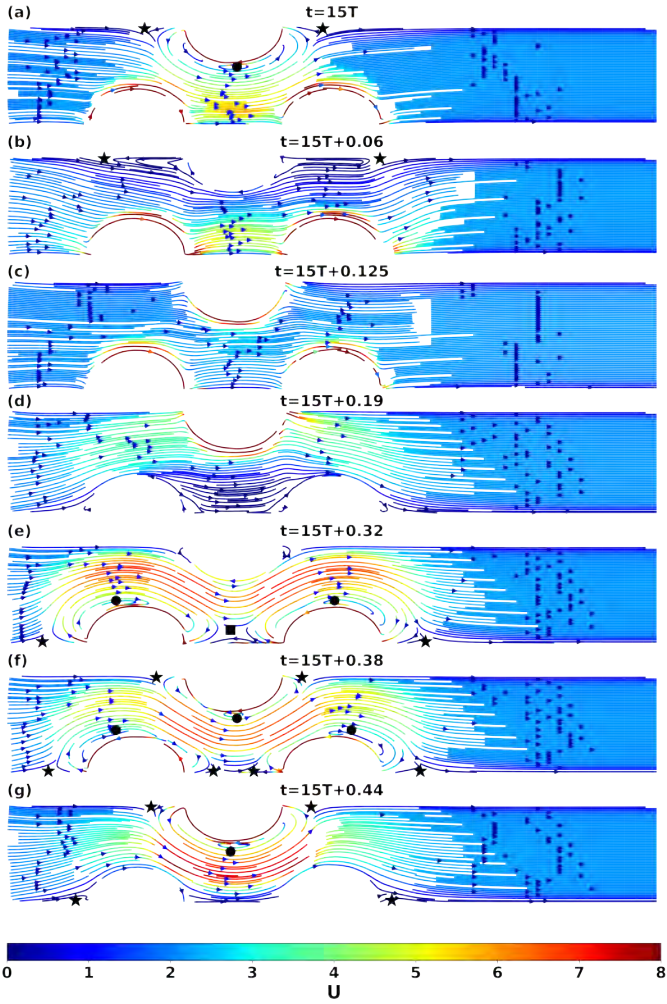


**Fig. 15** Illustration of flow topology for the largest yield stress case investigated ($\mathrm{Bn}_{\mathrm{bulk}} = 26.5, N = 0.75$) at several time instants indicated in the top inserts. The colour map refers to the magnitude of the flow speed $U$. The colour bounds have been purposely chosen to highlight features within the *"active"* flow region. The symbols highlight the special points of the flow: squares- hyperbolic points, circles - elliptical points, stars - parabolic points.

$$\lambda = \frac{\dot{\gamma} - \omega}{\dot{\gamma} + \omega} \tag{20}$$

where $\omega = \frac{\partial u_y}{\partial x} - \frac{\partial u_x}{\partial y}$ is the magnitude of the vorticity.

A pure straining flow corresponds to $\lambda \to 1$, a pure shear flow corresponds to $\lambda \to 0$ and the rigid body rotation corresponds to $\lambda \to -1$.

The analysis of the coupling between the flow type and the bulk Bingham number is summarized in Fig. 16. The dependence of the space and time

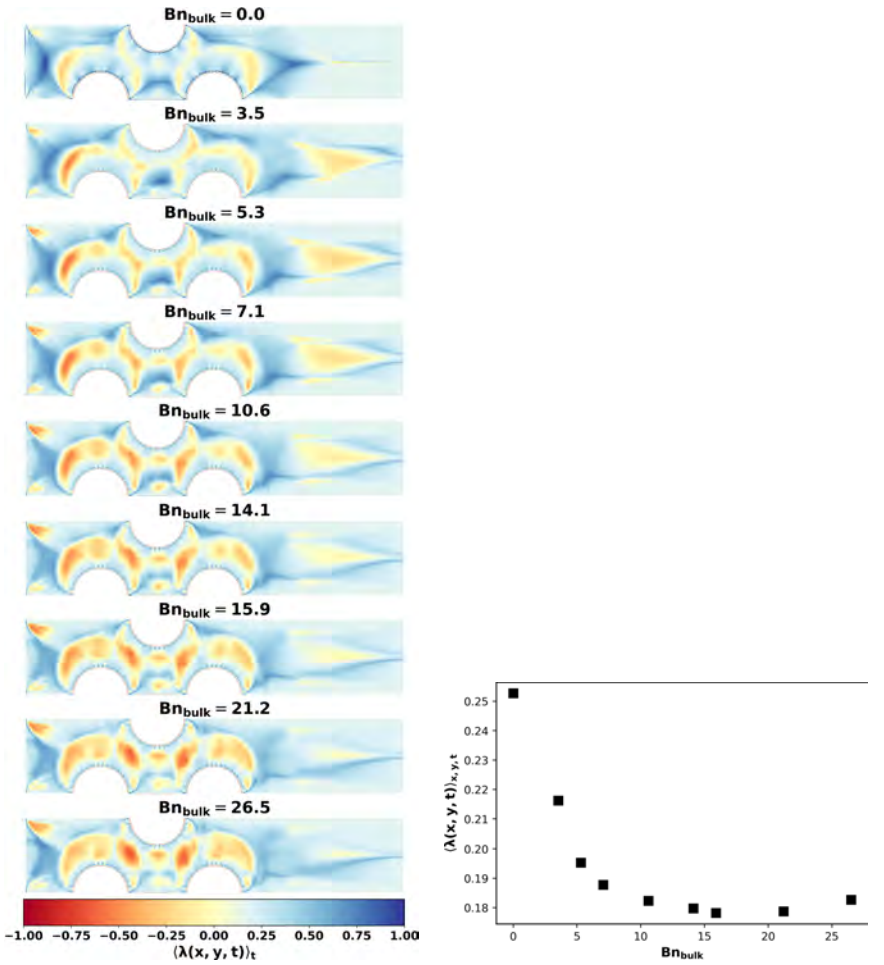


**Fig. 16** (a) Illustration of time averaged flow type parameter $\langle\lambda(x,y,t)\rangle_t$ computed for various bulk Bingham numbers detailed in the top inserts. (b) Dependence of the space and time averaged flow type parameter $\langle\lambda(x,y,t)\rangle_{x,y,t}$ on the bulk Bingham number $Bn_{bulk}$.

averaged flow parameter $\langle\lambda(x,y,t)\rangle_{x,y,t}$ is presented in Fig. 16(a) As the bulk Bingham number $\mathrm{Bn}_{bulk}$ is gradually increased, several tendencies in the distributions of the flow type parameter may be noticed. Regardless the value of the Bingham number, the regions of the flow close to the solid boundaries of the channel are dominated by shear. At zero Bingham, extensional zones are visible within the active flow region contained in between the rotating arc-walls. As the Bingham number is increased, a rigid body rotational component becomes visible in these zones. We believe this effect relates to the emergence

of solid material elements which do not deform but undergo a rigid body rotation. A systematic analysis of the sizes of these blobs will be presented in the upcoming Sec. 3.2.4 in connection to Fig. 20.

The dominance of a certain flow type be quantitatively assessed by monitoring the space and time averaged flow type parameter $\langle \lambda(x,y,t) \rangle_{x,y,t}$, Fig. 16(b). It is clear from this plot that the overall effect of the gradual increase of the Bingham number is a monotonic decrease of the extensional flow component which gets gradually replaced by the shear and the rigid body body translation.

### 3.2.2 Eulerian time correlations for various bulk Bingham numbers

As we have seen in Sec. 3.1 that the dynamics of the passive scalar in the bulk of the flow differs significantly from that observed within the boundary layers, we shall focus on the temporal auto-correlations of the flow fields and of the passive scalar within both the bulk of the flow and in the boundary layers and the relationship between the characteristic times of correlation and the bulk Bingham number $\mathrm{Bn}_{\mathrm{bulk}}$.

As a statistical measure of the mixing we compute the time auto-correlation functions of the passive scalar fluctuations for each value $y$ of transverse coordinate:

$$F\left(y,\tau/T\right)=\frac{\left\langle C'\left(y,t/T\right)C'\left(y,\left(t+\tau\right)/T\right)\right\rangle_{15\leq t/T\leq 20}}{C_{\mathrm{std}}(y)^2} \tag{21}$$

where $C'\left(y,t\right)=C\left(y,t\right)-\left\langle C(y,t)\right\rangle_{15\leq t/T\leq 20}$ and $C_{\mathrm{std}}(y)$ is the standard deviation of the concentration fluctuations at the transverse position $y$ computed over the last five periods of the mixing process. The correlation functions defined by Eq. 21 are computed using the last five periods of the space-time diagrams presented in Fig. 11 for each bulk Bingham number $\mathrm{Bn}_{\mathrm{bulk}}$ explored through the paper.

We illustrate in Fig. 17 time correlations averaged within the mixing boundary layers (the full lines) and within the bulk of the flow (dashed lines). For this computation we have used the space-time plots previously presented in Figs. 5, 8 for the Newtonian reference case and for the highest yield stress explored ($\mathrm{Bn}_{\mathrm{bulk}}=26.5, N=0.75$). As a reminder, the extent of the mixing boundary layer for each $\mathrm{Bn}_{bulk}$ was determined according to the procedure detailed in Sec. 3.1 and illustrated in Figs. 6, 9.

For both cases illustrated in Fig. 17, the passive scalar fluctuations are longer correlated within the mixing boundary layer (full lines) than in the bulk of the flow (dashed lines). The strongly oscillating tails of the correlation functions relate to the oscillatory nature of the external forcing. Next, using the averaged bulk/boundary correlation functions, we assess the corresponding correlation times $\tau_c$ as the first zero crossing marked by the full symbols in Fig. 17.

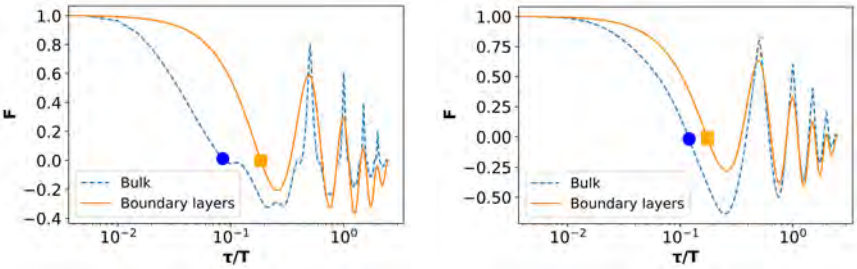


(a) (b)

**Fig. 17** Time auto-correlation functions of the passive scalar fluctuations averaged within the mixing boundary layers (full lines) and within the bulk of the flow (dashed lines) computed for the reference Newtonian case - panel (a) and for the highest yield stress case explored, $\mathrm{Bn_{bulk}} = 26.5$, $N = 0.75$ - panel (b). In both panels the full symbols mark the first zero crossing of the auto-correlation functions which defines the characteristic time of correlation of the passive scalar fluctuations.

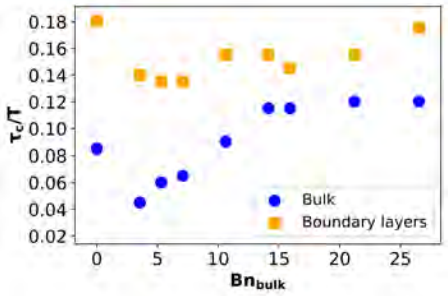


**Fig. 18** Dependence of the correlation times of the passive scalar fluctuations computed in the bulk of the flow (blue circles) and within the boundary layers (orange squares) on the bulk Bingham number $\mathrm{Bn_{bulk}}$.

We summarise the discussion of the temporal correlations of the passive scalar fluctuations in Fig. 18 where we display the dependence of correlation times computed within the bulk of the flow (squares) and within the boundary layers (circles) on the bulk Bingham number $\mathrm{Bn_{bulk}}$.

Within the mixing boundary layer the correlation times are practically insensitive to the bulk Bingham numbers - the squares in Fig. 18. The bulk correlation times, however increase with $\mathrm{Bn_{bulk}}$ reaching a plateau for high values of the yield stress. This corresponds to the progressive decrease of the mixing efficiency triggered by the presence of the yield stress illustrated in Fig. 12.

### 3.2.3 Spatial spectra of passive scalar fluctuations

The efficient mixing of a passive tracer in a hydrodynamic system relates to the progressive generation of small spatial scales of the distributions of the passive scalar by successive stretching and folding of fluid elements or, in other

words, to a cascade of passive scalar fluctuations [2] from the large (integral) scale down to the small (diffusive) scale. In the Fourier space this translates into a progressive decay of the power of the spatial fluctuations of the passive scalar concentration from small wave numbers corresponding to the integral scale at each the passive scalar is injected to high wave numbers which, in the case of efficient mixing, eventually reach the diffusive range.

We illustrate in Fig. 19 comparative computations of the spatial spectra of the fluctuations of the passive scalar for the reference Newtonian case - the curve labelled by a square, and for the highest yield stress case studied ($\mathrm{Bn}_{\mathrm{bulk}} = 26.5, N = 0.75$) - the curve labelled by a circle. For the reference Newtonian case a power law scaling $P \propto k^{-1}$ indicated by the dashed line in Fig. 19 is observed within a narrow band of wave numbers $k \in [20, 75]$. This algebraic scaling behavior is consistent with the Batchelor regime of mixing and originates from the temporal randomness and the spatial smoothness of the flow fields. For larger wave numbers a steeper decay of the spectrum of fluctuations is observed. A similar result has been reported by Jullien and her coworkers [Jullien et al(2000)Jullien, Castiglione, and Tabeling] and by [Jullien(2003)] and was attributed to the presence of the Taylor dispersion that alters the spatial distribution of the passive scalar fluctuations.

In the presence of yield stress a strikingly different spatial spectrum of the passive scalar observed. Within the narrow band of wave numbers where a power law decay was observed in the Newtonian case a sharp peak is observed in the presence if yield stress - the curve labelled by a circle in Fig. 19. This observation is consistent with the spatial periodicity of the passive scalar distributions observed along the horizontal direction for the yield stress case illustrated in Fig. 7.

On a purely intuitive basis so far, one can solely associate the emergence of the local maximum the power spectrum of the passive scalar fluctuations in the presence of the yield stress to an additional characteristic space scale associated to the viscoplastic behavior.

To put this hypothesis to a test, we focus in the upcoming section on the space-time dynamics of the un-yielded materials being transported past the *"active"* mixing zone.

### 3.2.4 Space-time dynamics of the yielded/un-yielded material elements at various Bingham numbers

While advancing downstream within the mixing channel, the material elements are yielded only partially and, at each axial position downstream, solid and fluid material elements coexist. As illustrated and discussed in Sec. 3.2.1, at the exit channel the central part of the flow is dominated by a rigid plug with a size that increases gradually as the bulk Bingham number is increased. Un-yielded flow regions do exist within the central part of the mixer in the vicinity of the arc-walls but their characteristic sizes are smaller than that of the central plug

[2] Not to be confused with the concept of *turbulent energy cascade* which is a hallmark of the inertial turbulence and does not make the object of the current investigation.

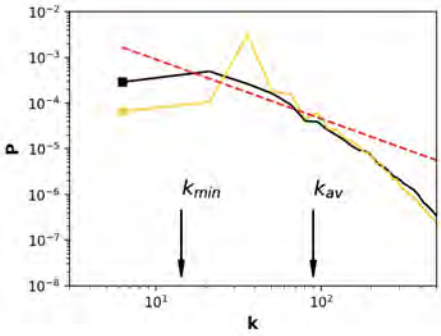


**Fig. 19** Spatial power spectra of the fluctuations of the passive scalar computed for the Newtonian reference case (the data set marked by a square) and for the largest yield stress case investigated. The dashed line is a guide for the eye, $k^{-1}$. The physical meaning of the spectral bounds $k_{\min}$, $k_{\max}$ indicated by the vertical arrows will be clarified in Sec. 3.2.4.

observed at the channel outlet. This can be seen in Fig. 3 which exemplifies the adaptive grid and the detection of the yield surfaces highlighted in red. This is because the maximal local rates of strain induced within the *"active"* mixing region by the external forcing are significantly larger that the strain rate at the exit of the channel, $\dot{\gamma}_{\text{central}} = K\dot{\gamma}_{\text{outlet}}$.

We focus in the following on the statistics of the sizes of the un-yielded blobs located within the central region of the flow (meaning that we disregard in this analysis the central plug formed at the channel's outlet which has been discussed already in Sec. 3.2.1 and illustrated in Fig. 13).

The additional mesh adaptivity based on the local value of the viscosity (see Fig. 3 and the description in Sec. 2.3) allows one to identify from each flow field the un-yielded zones defined by values of the local viscosity satisfying $\eta \geq 100$ and build up the statistics of their sizes solely accounting for the last five periods of the simulation.

We focus in the following on the statistics of sizes of such un-yielded blobs located within the *"active"* mixing zone located in between the rotating arc-walls. We illustrate several instantaneous distributions of such un-yielded elements in Fig. 20.

By a simple visual inspection of the data presented in Fig. 20 one may note that the size of the un-yielded material blobs is smaller than that of the of the central plug observed near the outlet and detailed in Figs. 13(a), 13(c). This was expected as the forcing Bingham number is smaller than the bulk Bingham number $\text{Bn}_f \leq \text{Bn}_{bulk}$ meaning that the yielding process is more effective within the *"active"* mixing zone than near the channel outlet. Near the channel inlet, a rigid plug is periodically formed (*e.g.* at $t/T = 15$ and $t/T = 16$) and destroyed (e.g. at $t/T = 15.5$ and $t/T = 16.5$). On the other hand, the central plug observed at the channel outlet changes much less during the mixing process. This is due to the fact that the *"active"* mixing zone is closer to the channel inlet than to the channel outlet. The periodicity in the dynamics of the un-yielded plugs is due to the periodicity of the external forcing imposed

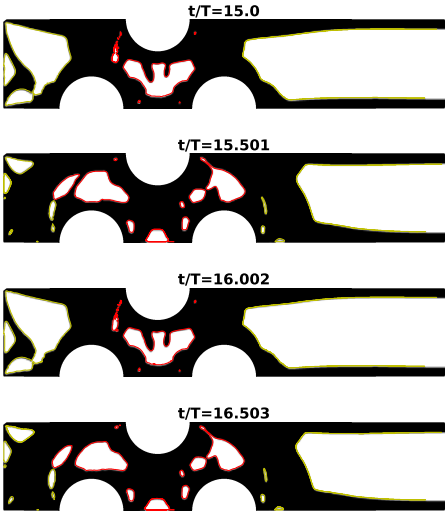


**Fig. 20** Illustration of un-yielded zones at $\mathrm{Bn_{bulk}} = 26.5$ and several time instants indicated in the top inserts. The solid blobs located within the *"active"* mixing zone and accounted for in the size statistics are highlighted by a red contour while the others are highlighted by a yellow contour.

by the motion of the arc-walls. We exemplify in Fig. 21 the probability density function (pdf) of the sizes $\Delta R$ of the un-yielded blobs located in *"active"* mixing zone for the highest yield stress case investigated, $\mathrm{Bn_{bulk}} = 26.5$. The characteristic size of each un-yielded blob has been computed using its area $A$ and perimeter $P$ as $\Delta R = \frac{4A}{P}$. The statistics of the un-yielded blob sizes have been computed on an ensemble of 5016 blobs detected during the last five periods of the mixing process. We observe an exponential tail of the pdf (see the full line in Fig. 21) but we do not have a clear theoretical understanding of this observation. The average size of the un-yielded blobs for this value of the bulk Bingham number is $\Delta R^{\mathrm{av}} = 0.071$, the median $\Delta R^{\mathrm{median}} = 0.03$ and the maximum blob size is $\Delta R^{\mathrm{max}} = 0.44$. The statistics of the blob sizes allow one to the define the two wave numbers highlighted by the vertical arrows in Fig. 19: $k_{\mathrm{min}} = \frac{2\pi}{\Delta R^{\mathrm{max}}}$, $k_{\mathrm{av}} = \frac{2\pi}{\Delta R^{\mathrm{av}}}$.

The analysis of the spectra of fluctuations of the passive scalar concentration presented in Sec. 3.2.3 combined with the analysis of the statistics of sizes of the un-yielded material elements passing through the *"active"* mixing region allows one to decode the physical picture of the dramatic loss of the mixing efficiency triggered by the presence of yield stress as follows.

The presence of un-yielded blobs brings into the hydrodynamic problem additional characteristic space scales related to the sizes of these blobs. In the Fourier space, this translates into the emergence of a band of wave numbers $[k_{\mathrm{min}}\ k_{\mathrm{av}}]$ where the cascade of passive scalar from the integral scale (defined by the width $W$ of the mixer) towards the diffusive range is truncated. This truncation of the energy transport of the passive scalar fluctuations from large

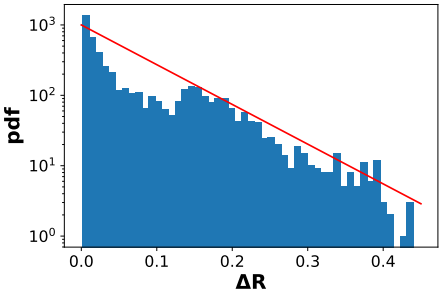


**Fig. 21** Probability density function of the sizes $\Delta R$ of the un-yielded blobs located in *"active"* mixing zone. The data refer to the highest yield stress case investigated, $\mathrm{Bn_{bulk}} = 26.5$. The line is a guide for the eye, $\mathrm{e}^{-13\Delta R}$.

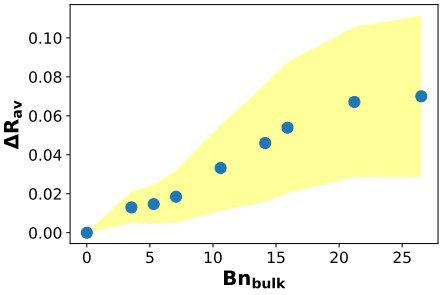


**Fig. 22** Dependence of the averaged size of the un-yielded blobs observed during the last five periods of the mixing process within the *"active"* mixing zone on the bulk Bingham number $\mathrm{Bn_{bulk}}$. The shaded area marks the standard deviation of the blob sizes around the mean value.

scales to small scales ultimately leads to the dramatic loss of mixing detailed in Sec. 3.1.

To conclude the analysis of the statistics of the sizes of un-yielded material elements, we present in Fig. 22 the dependence of the average blob size $\Delta R_{\mathrm{av}}$ on the bulk Bingham number $\mathrm{Bn_{bulk}}$. The shaded region indicates the standard deviation $\Delta R_{\mathrm{std}}$ of the blob sizes around their mean value. As $\mathrm{Bn_{bulk}}$ is gradually increased, both the average blob size $\Delta R_{\mathrm{av}}$ and the standard deviation $\Delta R_{\mathrm{std}}$ increase.

## 3.3 Lagrangian description of the flows at various Bingham numbers

The key physics underlying the mixing process triggered by the periodic forcing of the rotating arc-walls relates to stretching and folding of material elements down to spatial scales that are sufficiently small so the molecular diffusion may be effective in mixing. To better understand the interplay between the mixing and the yield stress behavior we turn our attention in this section to a Lagrangian frame analysis of the flow at various bulk Bingham numbers.

### 3.3.1 Statistics of the residence times

The most straightforward Lagrangian frame analysis of the flow relates to assessing the statistical distribution of the residence times of fluid particles within the flow channel. The residence time of a particle is defined as the time spent by the particle inside within the mixing channel [Nauman(2008)]. In the absence of laminar chaotic advection, the ensemble average of the residence times is controlled by the characteristic advection time $t_a = \frac{L}{U_{\max}}$. In the presence of laminar chaotic advection triggered by the periodic forcing of the flow, there will exist fluid particles that spend within the mixing channel a time significantly longer than the advection time $t_a$. We are interested in the following in understanding how the yield stress effects quantified by the bulk Bingham number $\mathrm{Bn}_{\mathrm{bulk}}$ influence the statistical distribution of the residence times.

To assess the statistics of the distribution of residence times we follow several steps. First, we consider $N = 132\,867$ particles evenly distributed (along a regular grid) within the flow channel at $t = 0$. The Lagrangian trajectories of each particle are obtained using the velocity fields $\boldsymbol{v}$ by numerical integration:

$$\begin{cases} \dot{\boldsymbol{x}}(t) = \boldsymbol{v}\left[\boldsymbol{x}(t), t\right], \\ \boldsymbol{x}(0) = \boldsymbol{x}_0, \end{cases}$$

where $\boldsymbol{x}$ is the position vector of the particle.

It is of particular importance here to account in the Lagrangian statistics for all the time steps which, bearing in mind that we deal with an open channel flow, can only be done be feeding back at the channel inlet the particles exiting the mixer which is equivalent to a periodic Lagrangian boundary condition. We present in Fig. 23 instantaneous positions of such Lagrangian tracers at several time instants (scaled by the period $T$ of the external forcing) indicated in the top inserts. The false colour map was added for the clarity of the visualisation and refers to the axial position $x$ of the tracers at $t = 0$ (see top panel). Second, to compute the statistical distributions of residence times, we focus on the dynamics of a small subset of Lagrangian tracers initially located within a narrow band of width $\Delta x = 0.1$ near the channel inlet ($x = -0.5$) and construct the statistical ensemble of residence times by computing the time each particle needs to exit the channel. As the exiting particles are continuously fed back through the channel inlet, we are able to account in the statistics of the residence times for all the time steps of the simulation which we believe it is crucial for a reliable statistical description of the residence times. For each particle that is fed back through the channel inlet the timer is reset to zero and the total time the particle spends within the channel is measured once more. This procedure allows to one build a statistically relevant ensemble of the residence times and ultimately compute the probability distributions of the residence times in the flow during the entire mixing process. We illustrate in Fig. 24 probability distributions of the residence times computed according to the procedure described above for various bulk Bingham numbers $\mathrm{Bn}_{\mathrm{bulk}}$

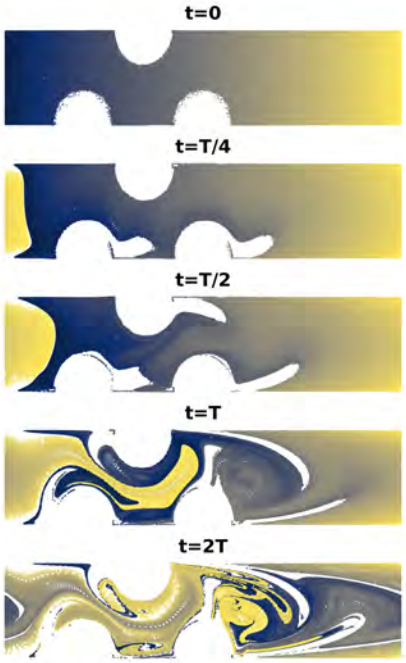


**Fig. 23** Instantaneous positions of Lagrangian tracers evenly distributed within the mixing channel at $t = 0$ at different time instants indicated in the top inserts. The false color map refers to the axial position $x$ of the initial tracers. The data refer to the reference Newtonian case, $\mathrm{Bn}_{\mathrm{bulk}} = 0, N = 1$.

indicated in the top inserts. The residence times are scaled by the period of the forcing, $t_{\mathrm{res}}/T$. The vertical dotted lines in each panel indicate the normalised advection time, $\frac{t_a}{T} = \frac{L}{U_{\max} T}$. For the Newtonian reference case ($\mathrm{Bn}_{\mathrm{bulk}} = 0, N = 1$) a broad distribution of residence times spanning an interval of roughly twelve periods of rotation is observed. Some particles spend within the mixing channel a time as long as 12 periods of rotation of the arc-walls which corroborates well with the good mixing observed in this case (see Fig. 5). As the Bingham number is gradually increased the tracers spend a significantly shorter time within the mixer and the statistical distribution of residence times narrows, Fig. 24. This corresponds to the dramatic loss of both the mixing efficiency and homogeneity of the mixture illustrated in Fig. 12. Quite interesting on the other hand is that, for a small value of the Bingham number ($\mathrm{Bn}_{\mathrm{bulk}} = 3.5$) and in the presence of a mild shear thinning behavior $N = 0.75$ one still obtains a broad distribution of residence times. As compared to the Newtonian reference case, the range $t/T \in [7, 11]$ of the histogram is now filled in more or less uniformly which is a signature of changes in the flow kinematics induced by the shear thinning behavior. This observation corroborates well with the good mixing behavior illustrated in Fig. 12 for this value of $\mathrm{Bn}_{\mathrm{bulk}}$.

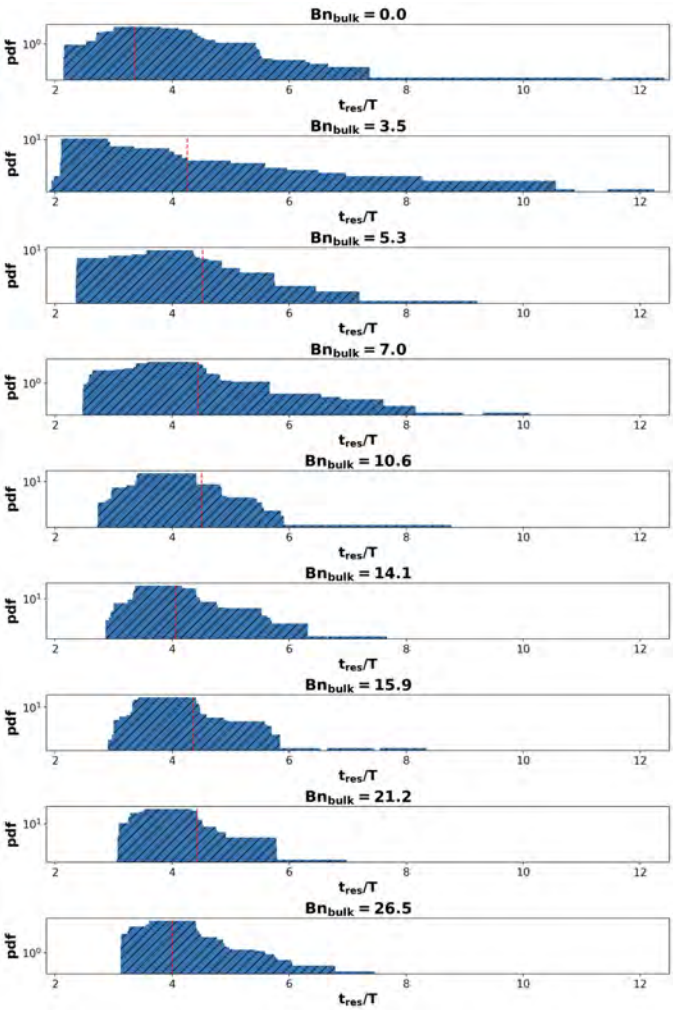


**Fig. 24** Histograms of the residence times for various bulk Bingham numbers $\mathrm{Bn}_{\mathrm{bulk}}$ indicated in the top inserts. In each panel the vertical dashed line marks the reduced advection time $t_a/T$.

As the the bulk Bingham number is increased past the critical value $\mathrm{Bn}_{\mathrm{bulk}}^{\mathrm{crit}} \approx 5$ which corresponds to the transition to poorly mixing flow states the pdf's of the residence time narrow progressively and their peak is shifted towards low values of $t_{\mathrm{res}}/T$. Corresponding to these flow states, in average, the particles spend a significantly shorter time within the mixing channel (of the order of $t_{\mathrm{res}}/T \approx 4$) than in the case of a fully developed chaotic flow. This is a first indication that the presence of yield stress inhibits the chaotic Lagrangian frame dynamics. A more systematic analysis of this issue is presented in the upcoming section.

### 3.3.2 Analysis of the Finite Time Lyapunov Exponents ($FTLE's$)

A quantitative measure of the degree of chaos of a hydrodynamic system is given by the largest Lyapunov exponent initially introduced by Dr. Aleksandr Mikhailovich Lyapunov (in a context seemingly unrelated to the chaotic dynamics of a hydrodynamic system) as a tool of studying the stability of solutions of ordinary differential equations describing the trajectories of rotating rigid bodies (with astronomy related applications in mind), [Lyapunov(1885)].

Given two fluid particles initially located at the positions $\boldsymbol{x}_0$ and $\boldsymbol{x}_0 + \delta\boldsymbol{x}_0$ the Lyapunov exponents $LE$ are defined by the logarithmic rate of separation of their trajectories with time:

$$LE = \lim_{t\to\infty} \lim_{||\delta\boldsymbol{x}_0||\to 0} \frac{1}{t} \log \frac{||\delta\boldsymbol{x}(t)||}{||\delta\boldsymbol{x}_0||} \tag{22}$$

where $||\delta\boldsymbol{x}(t)||$ is the distance between particles observed at the time instant $t$.

In practical cases when one needs to assess the degree of chaos of a hydrodynamic system based on the analysis of either experimentally measured or numerically computed flow fields the original definition of the Lyapunov exponents given by Eq. 22 is difficult to use in a physically meaningful manner: the infinite time limit can not be attained and nor can be infinitely small particle separations $\boldsymbol{x}_0$. A second (and perhaps the most prohibitive) difficulty in employing the original definition of the $LE's$ given by Eq. 22 relates to the finite size of the hydrodynamic system we investigate. Thus, within a finite time, initially close fluid particles might reach the viscoplastic boundary layers and get trapped within for long time. In this case the physical meaning of the logarithmic rate of separation becomes elusive and extra caution is needed while analysing such data.

A practical approach able to circumvent these difficulties is the *Finite Time Lyapunov Exponents* approach which, in a nutshell, consists of monitoring the rates of separation of a set of tracers initially located at the positions $\boldsymbol{x}_0$ during finite times and perform an appropriate statistical analysis which would asymptotically yield the $LE$'s. The first step of this approach consists of computing the flow map defined by:

$$\boldsymbol{F}_{t_0}^{t} : \boldsymbol{x}_0 \mapsto \boldsymbol{x}_t(t_0, \boldsymbol{x}_0), \tag{23}$$

where the finite time $t - t_0$ is chosen in relation to a characteristic time scale of the hydrodynamic system (the period of the external forcing in our case).

The right Cauchy-Green strain tensor is defined as:

$$\boldsymbol{C}_{t_0}^{t}(\boldsymbol{x}_0) = \left[\nabla \boldsymbol{F}_{t_0}^{t}(\boldsymbol{x}_0)\right]^{\mathrm{T}} \; \nabla \boldsymbol{F}_{t_0}^{t}(\boldsymbol{x}_0), \tag{24}$$

where T denotes the transpose. The eigenvalues $\lambda_i(\boldsymbol{x}_0;\ t_0, t)$ $(i = 1, 2)$ of $\boldsymbol{C}_{t_0}^{t}(\boldsymbol{x}_0)$, denoted by $\lambda_i(\boldsymbol{x}_0)$ for the simplicity of the notation satisfy:

$$0 < \lambda_1(\boldsymbol{x}_0) \leq 1 \leq \lambda_2(\boldsymbol{x}_0), \tag{25}$$

The finite-time Lyapunov exponents ($FTLE$) at a given position $\boldsymbol{x}_0$ over the time interval $[t_0, t]$ is defined as

$$\Lambda_{t_0}^{t}(\boldsymbol{x}_0) = \frac{1}{|t - t_0|} \log \sqrt{\lambda_2(\boldsymbol{x}_0)}. \tag{26}$$

If $t > t_0$ the $\Lambda_{t_0}^{t}(\boldsymbol{x}_0)$ is referred to as *"forward"* $FTLE$ while if $t < t_0$ as *"backward"* $FTLE$.

To compute the spatial distributions of $FTLE's$ we use the algorithms developed within the group of Professor George Haller and their Matlab implementation, [Onu et al(2015)Onu, Huhn, and Haller]. Here we summarise only briefly the main steps of the Haller approach. The first step consists of computing the flow map according to Eq. 23. This is done by computing the trajectories of the particles located at the positions $\boldsymbol{x}_0$ at the time instant $t_0$ during the time interval $[t_0, t]$ via numerical integration of the flow fields. For all FTLE's calculations illustrated herein we have used a fixed integration time, $ti = |t - t_0| = T/4$. Next, using the flow map we compute the right Cauchy-Green strain tensor according to Eq. 24 and its eigenvalues $\lambda_{1,2}$. Finally, the FTLE's are computing according to Eq. 26.

We exemplify for the Newtonian reference case ($\mathrm{Bn}_{\mathrm{bulk}} = 0, N = 1$) computations of the spatial distributions of the forward (top panel) and backward (bottom panel) $FTLE's$ in Fig. 25. We have purposely chosen for the illustration of these computations the time instant $t/T = 15.67$ which, as we are going to illustrate in the upcoming Fig. 27, corresponds to a maximum of the space averaged $FTLE's$.

For comparison, we illustrate in Fig. 26 distributions of the $FTLE's$ computed at the same time instant as for the Newtonian case for the highest yield stress case explored so far, ($\mathrm{Bn}_{\mathrm{bulk}} = 26.5, N = 0.75$). Corresponding to the plug flow observed at the channel outlet the $FTLE's$ are practically zero except for the narrow regions located near the channel boundaries which relate to the viscoplastic boundary layers highlighted in Fig. 13(c). This once more indicates that after advancing past the *"active"* mixing region the flow patterns are practically frozen. Yet the most striking differences with respect to the reference Newtonian case are observed within the *"active"* mixing region. In the viscoplastic case the $FTLE's$ within this region are significantly smaller than in the Newtonian case and the deformation is localised in the vicinity of the rotating arc-walls. This observation corroborates well with the observation of un-yielded material blobs within *"active"* mixing region exemplified in Fig. 20. Thus, one may conclude that the presence of such un-yielded material elements depletes the Lagrangian chaotic behavior which ultimately translates into the drastic decrease of the mixing efficiency illustrated in Fig. 12 and described in Sec. 3.1.

The computation of the spatial distributions of the FTLE's allows one to compute the maximum (over space) FTLE's $\Lambda^{\max}$ and the space averaged

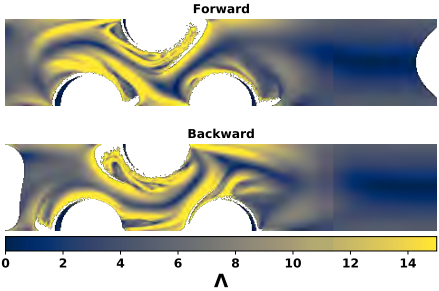


**Fig. 25** Example of computations of the spatial distributions of the forward (top panel) and backward (bottom panel) $FTLE's$ at $t/T = 15.67$. The data refer to the Newtonian reference case ($\mathrm{Bn}_{\mathrm{bulk}} = 0, N = 1$).

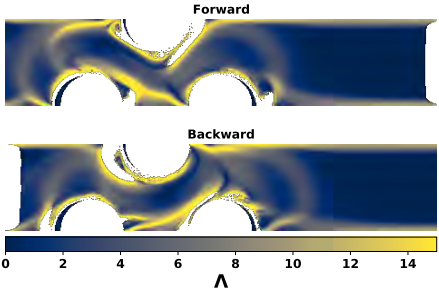


**Fig. 26** Example of computations of the spatial distributions of the forward (top panel) and backward (bottom panel) $FTLE's$ at $t/T = 15.67$. The data refer to the largest yield stress case explored ($\mathrm{Bn}_{\mathrm{bulk}} = 26.5, N = 0.75$).

value $\Lambda^{\mathrm{av}}$ at each time instant during the last five periods of the mixing process $t \in [15T, 20T]$. These quantities may be regarded as an indicator of the degree of chaos in the hydrodynamic system. We illustrate time series of $\Lambda^{\mathrm{max}}$ and $\Lambda^{\mathrm{av}}$ computed for the Newtonian reference case ($\mathrm{Bn}_{\mathrm{bulk}} = 0, N = 1$) in Fig. 27.

The dependence of the maximum (over the field of the field of view) and the space averaged Lyapunov exponents averaged during the five periods of the mixing process is shown in Fig. 28.

Corresponding to $\mathrm{Bn}_{\mathrm{bulk}} = 3.5$ one observes the largest values of $\Lambda^{\mathrm{max}}$ and $\Lambda^{\mathrm{av}}$. This corroborates well with the good mixing observed for this value of the bulk Bingham number in Fig. 12. As the bulk Bingham number is increased past this value a monotonic decrease of the FTLE's is observed which relates to the loss of the mixing efficiency. Quite interestingly, a linear decay of the space and time averaged FTLE's with the bulk Bingham number is observed in Fig. 28(a). We do not have a clear theoretical explanation of this result.

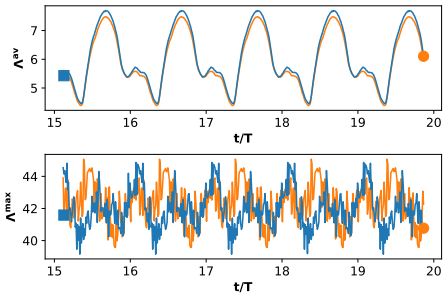


**Fig. 27** **Top**: Time series of the space averaged $FTLE's$, $\Lambda^{av}$. **Bottom**: Time series of the maximum (over space) FTLE's, $\Lambda^{max}$. In both panels the square marks the forward FTLE time series while the circle the backward one. The data refer to the Newtonian reference case ($\mathrm{Bn}_{\mathrm{bulk}} = 0, N = 1$).

# 4 On the possibility of increasing the mixing efficiency at high Bingham numbers

The results detailed in Sec. 3.1 indicate a significant role of the yield stress on the efficiency of the mixing process. This is mainly due to dramatic changes in the flow kinematics triggered by the presence of un-yielded material elements which, for the highest bulk Bingham number $\mathrm{Bn}_{\mathrm{bulk}}$ we have explored are not entirely yielded even in the central region of the flow where the stirring is the most effective. Moreover, even the material elements partially yield within the central part of the mixer, they quickly return to an un-yielded state while being transported little further downstream meaning that, when possible, the mixing process is mainly carried on within the central part of the mixer. From a practical perspective, we believe it is interesting to explore possibilities of alleviating the dramatic loss of mixing efficiency triggered by yield stress behavior. To this aspect we dedicate the current section.

## 4.1 On the possibility of increasing the mixing efficiency by the addition of a fourth stirring element

A first (and undoubtedly rather naive) solution is to add to the mixer a fourth rotating arc-wall on the same channel side as the top rotating arc-wall shown in Fig. 1. This is schematically illustrated in Fig. 29. As a forcing protocol, this fourth arc-wall will follow the motion of its closest neighbour located on the top side of the channel. Adding a fourth active element without modifying the forcing protocol (neither the forcing amplitude $K$ nor St) is not expected to trigger inertial instabilities and, consequently, its contribution to the global energetic cost associated to the mixing process remains reasonable.

The results on the mixing using the 4 rotating arc-walls variant of the mixer and the highest yield stress ($\mathrm{Bn}_{\mathrm{bulk}} = 26.5$, $N = 0.75$) are summarised in Fig. 30. These results need to be compared to those obtained for the 3 rotating arc-wall configuration illustrated in Fig. 8.

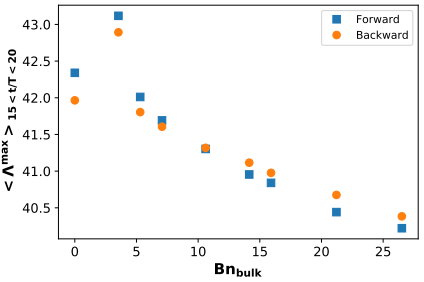


(a)

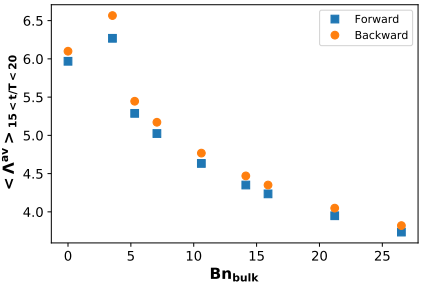


(b)

**Fig. 28** (a) Dependence of the maximum (over space) Lyapunov exponent averaged over the last five periods of the mixing process on the bulk Bingham number $\mathrm{Bn_{bulk}}$. (b) Dependence of the spaced averaged Lyapunov exponent averaged over the last five periods of the mixing process on the bulk Bingham number $\mathrm{Bn_{bulk}}$.

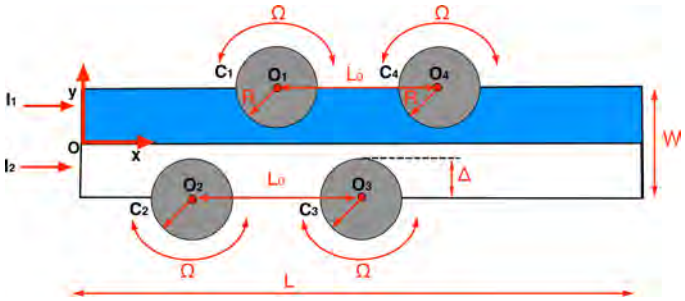


**Fig. 29** Schematic representation of the 4 rotating arc-walls mixer (in scale).

As compared to the result obtained with the three rotating arc-walls configuration, the addition of a fourth rotating arc-wall leads to a modest improvement in the mixing efficiency in the sense that the steady state value of the mixing indicator now drops to $C_{\mathrm{std}}^{\mathrm{av}} = 0.285$ from $C_{\mathrm{std}}^{\mathrm{av}} = 0.3$, Fig. 30(b).

A more significant advantage of adding a fourth rotating arc-wall relates to the overall homogeneity of the mixture. Whereas for the initial configuration

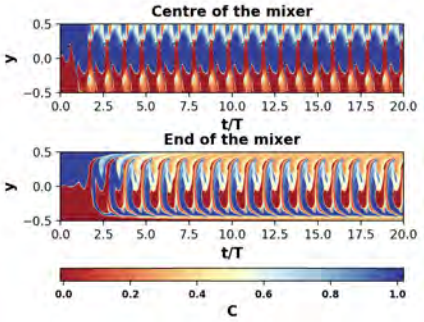


(a)

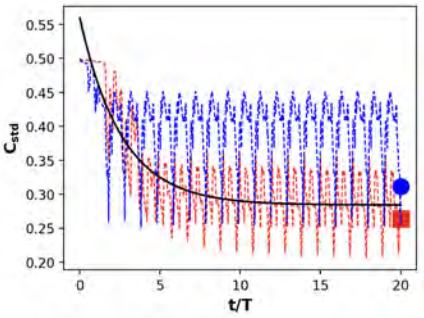


(b)

**Fig. 30** (a) Space time plots obtained for the highest yield stress case ($\mathrm{Bn_{bulk}} = 26.5$, $N = 0.75$) at the centre of 4 rotating arc-walls mixer (top panel) and at its exit of the mixer (bottom panel). (b) Time series of the mixing indicator $C_{\mathrm{std}}$ obtained for the highest yield stress case ($\mathrm{Bn_{bulk}} = 26.5$, $N = 0.75$) at the centre of the mixer of the 4 rotating arc-walls mixer (circle) and at the exit of the mixer (square). The full line is an exponential fitting function.

it was obtained $\delta C_{\mathrm{std}} = 0.045$ we now obtain $\delta C_{\mathrm{std}} = 0.032$ meaning the homogeneity of the mixture increased by roughly 25%.

## 4.2 On the possibility of increasing the mixing efficiency increasing the strength of the external forcing

An alternative solution to improving the poor mixing observed in the presence of the yield stress consists of gradually increasing the strength of the external forcing, (the amplitude $\Omega_0$ of the rotating drums) while keeping the initial geometric configuration and the main flow parameters unchanged. This method should be employed with caution as it leads to an increase of the forcing Reynolds number $\mathrm{Re}_f$ and trigger inertial instabilities which would lead to a drastic increase of the flow resistance which, from an energetic standpoint, is undesirable in the context of practical applications.

To test this idea, we have gradually increased the forcing amplitude from $K = 16$ (the value used through the bulk of the paper which corresponds to

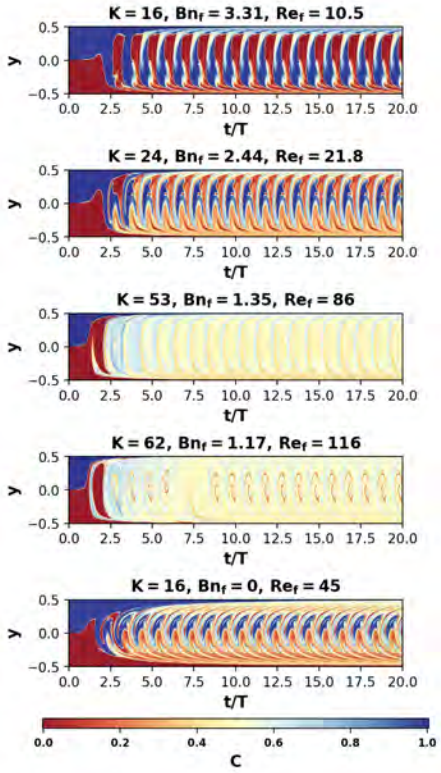


**Fig. 31** Space-time diagrams of the mixing process at the exit of the mixer for various forcing schemes summarised in the top inserts (see the text for the description of the numerical setting). The bottom panel refers to the reference Newtonian case already discussed through the manuscript.

$\mathrm{Re}_f = 45$ for the reference Newtonian case and $\mathrm{Re}_f = 10.5$ for the largest yield stress case investigated through the paper) to $K = 62$. As we are interested here only in the largest yield stress case investigated $\mathrm{Bn}_{\mathrm{bulk}} = 26.5$, the largest forcing Reynolds number is $Re_f = 116$.

To quantitatively assess the improvement of the mixing obtained by increasing the strength of the stirring, we present in Fig. 31 the corresponding space time diagrams acquired at the exit of the mixer. For reference, the bottom space time diagram corresponds to the Newtonian case already discussed through the paper.

The time series of the mixing indicator corresponding to all the cases illustrated in Fig. 31 are displayed together in panel **(a)** of Fig. 32.

The dependence of the plateau value $C_{\mathrm{std}}^{\mathrm{av}}$ of the time series of the mixing indicator on the forcing Reynolds number $\mathrm{Re}_f$ is presented in panel **(b)** of Fig. 32.

As the forcing Reynolds number is gradually increased above the value $\mathrm{Re}_f \approx 50$ a better is observed in terms of both the plateau value of the time

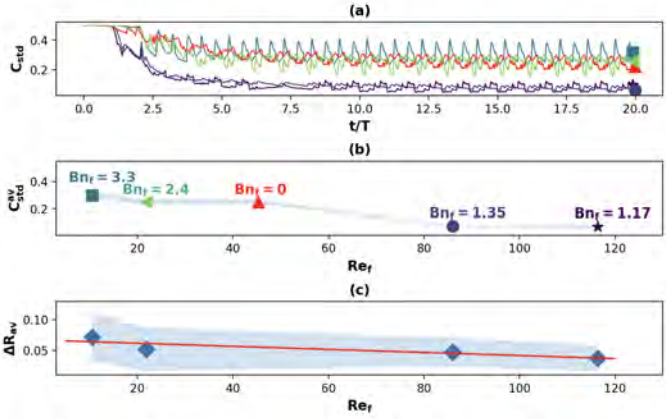


**Fig. 32** **(a)** Time series of the mixing indicator $C_{\text{std}}$ obtained at the exit of the mixer for the forcing schemes illustrated in Fig.31: **(b)** Dependence of the mixing efficiency parameter $C^{\text{av}}_{\text{std}}$ on the forcing Reynolds number $\text{Re}_f$. The corresponding forcing Bingham numbers $\text{Bn}_f$ are indicated in the text annotations. The shaded regions highlight the level of fluctuations of the mixing indicator around its dynamical steady state value, $\delta C_{\text{std}}$. **(c)** Dependence of the averaged size of yielded blobs $\Delta R_{\text{av}}$ on the forcing Reynolds number $\text{Re}_f$ for a fixed bulk Bingham number $\text{Bn}_{\text{bulk}} = 26.5$ and a fixed bulk Reynolds number $\text{Re}_{\text{bulk}} = 0.05$. The full line is a linear fit. In panels **(a, b)** the symbols refer to the parameters of the external forcing: square - $K = 16$, $\text{Bn}_f = 3.3$, $\text{Re}_f = 10.5$, left triangle - $K = 24$, $\text{Bn}_f = 2.4$, $\text{Re}_f = 21.8$, circle - $K = 53$, $\text{Bn}_f = 1.35$, $\text{Re}_f = 86$, star - $K = 62$, $\text{Bn}_f = 1.17$, $\text{Re}_f = 116$, up triangle - $K = 16$, $\text{Bn}_f = 0$, $\text{Re}_f = 45$.

series of the mixing indicator and its level of fluctuations around its mean, already stated through the paper is an indicator of the homogeneity of the mixture. Quite interestingly, increasing $\text{Re}_f$ past $\text{Re}_f \approx 80$ does not seem to improve the mixing any further.

Further insights into the increase of the mixing efficiency and the homogeneity of the mixture upon increasing the forcing Reynolds number may be gained by monitoring the size $\Delta R_{\text{av}}$ of the solid blobs averaged over the last five periods of the mixing process within the *"active"* mixing region, panel **(c)** of Fig. 32. A monotonic and roughly linear decrease of average size of unyielded blobs $\Delta R_{\text{av}}$ with $\text{Re}_f$ is observed. Thus, upon a graduate increase of the forcing strength, the spectral peak which blocks the energy transfer from the integral scale to the diffusive scales illustrated in Fig. 19 tends to vanish corresponding to a full yielding of the material in *"active"* mixing region which explains why the efficient mixing is gradually restored.

# 5 Conclusions, outlook

A systematic numerical study of the impact of viscoplastic rheological behavior on the active mixing within a rotating arc-walls channel recently proposed in Ref. [El Omari et al(2021)El Omari, Younes, Burghelea, Castelain, Moguen, and Le Guer] by laminar chaotic advection is presented. The central finding of the paper

detailed in Sec. 3.1 is that the presence of yield stress drastically alters the spatial distributions of the concentration of the passive scalar Figs. 4, 7 as well as the space-time dynamics of the concentration distributions Figs. 5(a), 8(a).

As the yield stress effects are gradually increased past a critical value of the bulk Bingham number $\mathrm{Bn}^{c}_{\mathrm{bulk}} \approx 5$ while maintaining the same flow conditions (inflow speed, Pe, forcing ratio $K$) and stirring protocol an abrupt and significant decrease of both the mixing efficiency and the homogeneity of the mixture is observed, Fig. 12. The non-monotonic behavior of the mixing efficiency may be understood in terms of a competition between two phenomena with opposite trends observed when $\mathrm{Bn}_{bulk}$ is gradually increased: the monotonic decrease of the width of the mixing boundary layer, Fig. 10 and the monotonic increase of the average sizes of the un-yielded blobs, Fig. 22.

To explore the physical reasons underlying this observation a detailed characterisation of the flows at various bulk Bingham numbers $\mathrm{Bn}_{\mathrm{bulk}}$ was performed in both an Eulerian Sec. 3.2 and a Lagrangian frame of reference Sec. 3.3.

The first part of the Eulerian flow description aims understanding the relationship between the flow topology and the yield stress behavior of the material. At the channel outlet a central rigid plug with a size that increases as $\mathrm{Bn}_{\mathrm{bulk}}$ increases is observed, Fig. 13. Two observations are of particular relevance here. First, at the channel outlet the time averaged cross flow velocity is significantly smaller than the time averaged axial velocity. Second, while fluctuations of the small cross-flow velocity component may be observed, no fluctuations of the axial component are visible. These observations indicate that in the presence of yield stress the material elements are *"frozen"* after passing through the *"active"* flow region. Thus, if some mixing may be triggered in the flow in the presence of yield stress, this may solely happen within *"active"* flow region. As illustrated in Fig. 13(c) widths of the top and bottom viscoplastic boundary layers observed at the channel outlet follow a power law scaling with the bulk Bingham number ($\propto \mathrm{Bn}_{\mathrm{bulk}}^{-\frac{N}{N+1}} = \mathrm{Bn}_{\mathrm{bulk}}^{-0.428}$) $\mathrm{Bn}_{\mathrm{bulk}}$ in a good agreement with theoretical predictions of Piau and Debiane, [Piau and Debiane(2004)].

Through the second part of the Eulerian description of the flow fields we have focused on the Eulerian flow topology qualitatively assessed by the stream lines. Whereas for the reference Newtonian case illustrated in Fig. 14 the flow topology is consistent with an efficient stretching and folding of material elements which ultimately lead to efficient mixing, in the yield stress case illustrated in Fig. 15 one can note that these dynamics are significantly altered: the parabolic points get significantly closer to rotating arc-walls, the characteristic size of the elliptic zones decreases and the hyperbolic point is now barely visible. These observations provide a first set of physical insights into the mechanisms responsible for the loss of mixing efficiency triggered by the yield stress behavior in terms of a dramatic change of the flow structure within the *"active"* mixing region.

A discussion of the Eulerian correlation functions of the passive scalar fluctuations is presented in Sec. 3.2.2. The passive scalar fluctuations are longer correlated within the mixing boundary layers than in the bulk of the flow, Fig. 17. The characteristic times of correlations are practically insensitive to $\mathrm{Bn}_{\mathrm{bulk}}$ within the mixing boundary layers but increase up to a plateau value within the bulk of the flow, Fig. 18. This increase is directly related to the decrease of the mixing efficiency observed upon increasing $\mathrm{Bn}_{\mathrm{bulk}}$, Fig. 12.

A key element in understanding the physics underlying the dramatic loss of the mixing efficiency in the presence of yield stress comes from the analysis of the spatial spectra of the fluctuations of the passive scalar concentration summarised in Fig. 19. The efficient mixing observed in the Newtonian case relates to an algebraic decay of the power spectrum, $P \propto k^{-1}$. Bearing in mind that the flows are spatially smooth and random in time, this algebraic scaling is a hallmark of the so-called Batchelor regime of mixing [Batchelor(1959)]. In the presence of yield stress such spectral decay region is no longer observed and a sharp peak of the power is observed within this range of wave numbers. Whereas it was obvious from the illustrations presented in Fig. 7 that this peak relates to a spatial periodicity (along the $x$ axis) of the passive scalar distributions understanding the physical natures of the bounds $k_{\mathrm{min}}$, $k_{\mathrm{av}}$ required an additional analysis.

By taking full advantage of the adaptive grid capabilities of the Gerris flow solver and adding an additional refinement of the computational grid based on the local value of the viscosity, we have detected at each time step the yield surface Fig. 20 which allowed one to compute the probability density functions of the sizes of un-yielded material elements, Fig. 21 and finally monitor the dependence of the time averaged un-yielded blob size to the bulk Bingham number, Fig. 22. This additional analysis helped *"deciphering"* the physical origins of the spectral bounds $k_{\mathrm{min}}$, $k_{\mathrm{av}}$ of the spectrum presented in Fig. 19: $k_{\mathrm{av}}$ is set by the time averaged size of the un-yielded blobs $k_{\mathrm{av}} = 2\pi/\Delta R_{\mathrm{av}}$ whereas $k_{\mathrm{min}}$ is set by the maximal size of the un-yielded blobs, $k_{\mathrm{min}} = 2\pi/\Delta R_{\mathrm{max}}$.

The Lagrangian flow description detailed in Sec. 3.3 brings additional insights into the mixing problem we study. Through the first part of the Lagrangian analysis (Sec. 3.3.1) we have focused on the statistics of the residence times of a set of evenly distributed tracers by the flow, Fig. 23. As the bulk Bingham number is gradually increased, the probability distributions of the residence times narrow which indicates that the yield stress behaviors inhibits the laminar chaotic advection of the tracers, Fig. 24.

A more rigorous Lagrangian frame analysis of the flow is presented in Sec. 3.3.2 in terms of computations of the space time dynamics of the FTLE's. As compared to the Newtonian reference case illustrated in Fig. 25, the spatial distributions of both the forward and the backward FTLE's is substantially different in the presence of yield stress, Fig. 26. Due to the presence of the un-yielded plug observed at the channel outlet in the presence of yield stress, no deformation is observed: both the forward and the backward FTLE's are

practically zero. As compared to the reference Newtonian case the most dramatic differences are observed within the *"active"* mixing region: the FTLE's remain large only within narrow regions located in the vicinity of the rotating arc-walls whereas within the central part of the mixer (where the efficient mixing is expected to carried on) they are nearly zero. This corroborates well with the significant changes observed in the flow topology in Fig. 15 which in turn originates from the presence of un-yielded blobs within the *"active"* mixing region, Fig. 20.

Due to the oscillatory forcing of the flow both the spatial average and the maxima of the FTLE are time periodic, Fig. 27. As the Bingham number is gradually increased past the critical bulk Bingham number $\mathrm{Bn}^{c}_{\mathrm{bulk}}$ corresponding to the loss of mixing efficiency both the time averaged maximal (over the field of view) FTLE $\langle \Lambda^{\max} \rangle$ and the space-time averaged FTLE (which may be regarded as global indicators of the degree of chaos of the hydrodynamic system) decrease, Fig. 28. The central message of the Lagrangian frame analysis is that the presence of yield stress inhibits the chaotic nature of the flow.

Finally, two rather basic solutions able to alleviate to some extent the loss of mixing efficiency triggered by the yield stress are discussed in Sec. 4. The first attempt consisted of adding a fourth stirring element while maintaining the same flow conditions and deliberately focusing on the highest yield stress investigated ($\mathrm{Bn}_{\mathrm{bulk}} = 26.5$, $N = 0.75$), Sec. 4.1. The improvement of the mixing efficiency defined by the plateau value $C^{\mathrm{av}}_{\mathrm{std}}$ of the time series of the mixing indicator obtained by the addition of a fourth stirring element is minimal but the overall homogeneity of the mixture defined by the level of fluctuations $\delta C_{\mathrm{std}}$ of the mixing indicator is improved, Fig. 30.

A more efficient solution of increasing the mixing efficiency is discussed in Sec. 4.2 and consists of gradually increasing the strength of the external forcing $K$. This method should employed with a fair amount of caution as it leads to an increase of the forcing Reynolds number $\mathrm{Re}_f$ which may trigger inertial instabilities adding thus a penalty on the energetic efficiency of the mixer.

As the $\mathrm{Re}_f$ is gradually increased in the range $\mathrm{Re}_f \in [10, 120]$ a roughly three-fold increase of the mixing efficiency is observed, Fig. 32(**(a,b)**). This improvement is directly related to the size of the un-yielded material elements passing through the *"active"* mixing which decreases (more or less linearly) with $\mathrm{Re}_f$, Fig. 32(**(c)**).

In closing, this study might open new avenues along two distinct tracks. Along a fundamental line, we believe it may trigger further theoretical studies on the coupling between yield stress rheological behavior and laminar chaotic advection. From a practical perspective, this study may trigger further engineering developments able to alleviate the dramatic loss of mixing associated with the yield stress behavior.

## Acknowledgements

We are particularly indebted to the anonymous first referee for prompting us to explain in more detail the non-monotonic evolution of the overall mixing efficiency with the bulk Bingham number.

## Declarations

- **Funding**
  The authors acknowledge the financial support from the French research Program No. $ANR-16-CE06-0003$ through the $NaiMYS$ project (Novel active inline Mixer for Yield Stress fluids).
- **Conflict of interest/Competing interests**
  We hereby declare having no conflicts of interests.
- **Ethics approval**
  Not applicable
- **Consent to participate**
  Not applicable
- **Consent for publication**
  Not applicable
- **Availability of data and materials** Not applicable
- **Code availability**
  The codes are available upon reasonable request.
- **Authors' contributions**
  The project was designed by T. B. The numerical simulations have been entirely designed, implemented and conducted by T. B. The post processing of the numerical data was jointly performed by T. B., E. Y and Y. M. The paper and the rebuttal letters were written by T. B.

## References

[Aref(1984)] Aref H (1984) Stirring by chaotic advection. J Fluid Mech 143:1–21. https://doi.org/10.1017/S0022112084001233

[Arratia et al(2006)Arratia, Kukura, Lacombe, and Muzzio] Arratia PE, Kukura J, Lacombe J, et al (2006) Mixing of shear-thinning fluids with yield stress in stirred tanks. AIChE J 52(7):2310–2322. https://doi.org/10.1002/aic.10847, URL https://doi.org/10.1002/aic.10847

[Balmforth et al(2014)Balmforth, Frigaard, and Ovarlez] Balmforth NJ, Frigaard IA, Ovarlez G (2014) Yielding to stress: Recent developments in viscoplastic fluid mechanics. Annu Rev Fluid Mech 46(1):121–146. https://doi.org/10.1146/annurev-fluid-010313-141424, URL https://doi.org/10.1146/annurev-fluid-010313-141424

[Batchelor(1959)] Batchelor GK (1959) Small-scale variation of convected quantities like temperature in turbulent fluid

part 1. general discussion and the case of small conductivity. J Fluid Mech 5(1):113–133. https://doi.org/10.1017/S002211205900009X, URL https://www.cambridge.org/core/article/small-scale-variation-of-convected-quantities-like-temperature-in-turbulent-fluid-par A8AEA175A906F98CDDB0F9ED146BB9FE

[Bonn and Denn(2009)] Bonn D, Denn MM (2009) Yield stress fluids slowly yield to analysis. Science 324(5933):1401–1402. https://doi.org/10.1126/science.1174217, URL http://science.sciencemag.org/content/324/5933/1401, https://arxiv.org/abs/http://science.sciencemag.org/content/324/5933/1401.full.pdf

[Bonn et al(2017)Bonn, Denn, Berthier, Divoux, and Manneville] Bonn D, Denn MM, Berthier L, et al (2017) Yield stress materials in soft condensed matter. Rev Mod Phys 89:035,005. https://doi.org/10.1103/RevModPhys.89.035005, URL https://link.aps.org/doi/10.1103/RevModPhys.89.035005

[Boujlel et al(2016)Boujlel, Pigeonneau, Gouillart, and Jop] Boujlel J, Pigeonneau F, Gouillart E, et al (2016) Rate of chaotic mixing in localized flows. Phys Rev Fluids 1(3). https://doi.org/10.1103/physrevfluids.1.031301, URL https://doi.org/10.1103/physrevfluids.1.031301

[Burghelea(2005)] Burghelea T (2005) Elastic turbulence and mixing in a dilute polymer solution. PhD thesis, Feinberg Graduate School of the Weizmann Institute of Science

[Burghelea et al(2004a)Burghelea, Segre, Bar-Joseph, Groisman, and Steinberg] Burghelea T, Segre E, Bar-Joseph I, et al (2004a) Chaotic flow and efficient mixing in a microchannel with a polymer solution. Phys Rev E 69(6):066,305–8

[Burghelea et al(2004b)Burghelea, Segre, and Steinberg] Burghelea T, Segre E, Steinberg V (2004b) Mixing by polymers: Experimental test of decay regime of mixing. Phys Rev Lett 92(16):164,501–4

[Coussot(2014)] Coussot P (2014) Yield stress fluid flows: A review of experimental data. J Non-Newtonian Fluid Mech 211:31 – 49. https://doi.org/https://doi.org/10.1016/j.jnnfm.2014.05.006, URL http://www.sciencedirect.com/science/article/pii/S0377025714000895

[Duplat and Villermaux(2008)] Duplat J, Villermaux E (2008) Mixing by random stirring in confined mixtures. J Fluid Mech 617:51–86. https://doi.org/10.1017/S0022112008003789

[El Omari et al(2021)El Omari, Younes, Burghelea, Castelain, Moguen, and Le Guer] El Omari K, Younes E, Burghelea T, et al (2021) Active chaotic mixing in a channel with rotating arc-walls. Phys Rev Fluids 6:024,502. https://doi.org/10.1103/PhysRevFluids.6.024502, URL https://link.aps.org/doi/10.1103/PhysRevFluids.6.024502

[Eyink and Sreenivasan(2006)] Eyink GL, Sreenivasan KR (2006) Onsager and the theory of hydrodynamic turbulence. Rev Mod Phys 78:87–135. https://doi.org/10.1103/RevModPhys.78.87, URL https://link.aps.org/doi/10.1103/RevModPhys.78.87

[Fereday and Haynes(2004)] Fereday DR, Haynes PH (2004) Scalar decay in two-dimensional chaotic advection and Batchelor-regime turbulence. Phys Fluids 16(12):4359–4370. https://doi.org/10.1063/1.1807431, URL https://doi.org/10.1063/1.1807431

[Fereday et al(2002)Fereday, Haynes, Wonhas, and Vassilicos] Fereday DR, Haynes PH, Wonhas A, et al (2002) Scalar variance decay in chaotic advection and Batchelor-regime turbulence. Phys Rev E 65(3). https://doi.org/10.1103/physreve.65.035301, URL https://doi.org/10.1103/physreve.65.035301

[Frigaard(2019)] Frigaard I (2019) Simple yield stress fluids. Curr Opin Colloid Interface Sci 43:80–93. https://doi.org/10.1016/j.cocis.2019.03.002, URL https://doi.org/10.1016/j.cocis.2019.03.002

[Fuller and Leal(1981)] Fuller G, Leal L (1981) The effects of conformation-dependent friction and internal viscosity on the dynamics of the nonlinear dumbbell model for a dilute polymer solution. Journal of Non-Newtonian Fluid Mechanics 8(3):271–310. https://doi.org/https://doi.org/10.1016/0377-0257(81)80026-2, URL https://www.sciencedirect.com/science/article/pii/0377025781800262

[Gouillart et al(2008)Gouillart, Dauchot, Dubrulle, Roux, and Thiffeault] Gouillart E, Dauchot O, Dubrulle B, et al (2008) Slow decay of concentration variance due to no-slip walls in chaotic mixing. Phys Rev E 78:026,211. https://doi.org/10.1103/PhysRevE.78.026211, URL https://link.aps.org/doi/10.1103/PhysRevE.78.026211

[Jullien(2003)] Jullien MC (2003) Dispersion of passive tracers in the direct enstrophy cascade: Experimental observations. Phys Fluids 15(8):2228–2237. https://doi.org/10.1063/1.1585030, URL https://doi.org/10.1063/1.1585030, https://arxiv.org/abs/https://doi.org/10.1063/1.1585030

[Jullien et al(2000)Jullien, Castiglione, and Tabeling] Jullien MC, Castiglione P, Tabeling P (2000) Experimental observation of Batchelor dispersion of passive tracers. Phys Rev Lett 85:3636–3639. https://doi.org/10.1103/PhysRevLett.85.3636, URL https://link.aps.org/doi/10.1103/PhysRevLett.85.3636

[Kraichnan(1968)] Kraichnan RH (1968) Small-scale structure of a scalar field convected by turbulence. Phys Fluids 11(5):945–953. https://doi.org/10.1063/1.1692063, URL https://aip.scitation.org/doi/abs/10.1063/1.1692063, https://arxiv.org/abs/https://aip.scitation.org/doi/pdf/10.1063/1.1692063

[Lester and Chryss(2019)] Lester DR, Chryss A (2019) Topological mixing of yield stress materials. Phys Rev Fluids 4(6). https://doi.org/10.1103/physrevfluids.4.064502, URL https://doi.org/10.1103/physrevfluids.4.064502

[Lyapunov(1885)] Lyapunov AM (1885) On the stability of ellipsoidal figures of equilibrium of a rotating fluid (in Russian). Bulletin Astronomique 1885

[Nauman(2008)] Nauman EB (2008) Residence time theory. Ind Eng Chem Res 47(10):3752–3766. https://doi.org/10.1021/ie071635a, URL https:

//doi.org/10.1021/ie071635a, https://arxiv.org/abs/https://doi.org/10.1021/ie071635a

[Nguyen and Boger(1992)] Nguyen QD, Boger DV (1992) Measuring the flow properties of yield stress fluids. Annu Rev Fluid Mech 24(1):47–88

[Onu et al(2015)Onu, Huhn, and Haller] Onu K, Huhn F, Haller G (2015) LCS Tool: A computational platform for Lagrangian coherent structures. J Comput Sci 7:26–36

[Ottino(1989)] Ottino JM (1989) The kinematics of mixing: stretching, chaos, and transport. Cambridge University Press

[Papanastasiou(1987)] Papanastasiou TC (1987) Flows of materials with yield. J Rheol 31(5):385–404

[Piau and Debiane(2004)] Piau JM, Debiane K (2004) Adhesive or slippery flat plate viscoplastic boundary layer for a shear-thinning power-law viscosity. J Non-Newtonian Fluid Mech 117:97–107

[Popinet(2003)] Popinet S (2003) Gerris: a tree-based adaptive solver for the incompressible Euler equations in complex geometries. J Comput Phys 190(2):572–600. https://doi.org/https://doi.org/10.1016/S0021-9991(03)00298-5, URL https://www.sciencedirect.com/science/article/pii/S0021999103002985

[Popinet(2009)] Popinet S (2009) An accurate adaptive solver for surface-tension-driven interfacial flows. J Comput Phys 228(16):5838–5866

[Popinet(2015)] Popinet S (2015) A quadtree-adaptive multigrid solver for the Serre–Green–Naghdi equations. J Comput Phys 302:336–358

[Stroock et al(2002)Stroock, Dertinger, Ajdari, Mezić, Stone, and Whitesides] Stroock AD, Dertinger SKW, Ajdari A, et al (2002) Chaotic mixer for microchannels. Science 295(5555):647–651. https://doi.org/10.1126/science.1066238, URL https://www.science.org/doi/abs/10.1126/science.1066238, https://arxiv.org/abs/https://www.science.org/doi/pdf/10.1126/science.1066238

[Thompson and Soares(2016)] Thompson RL, Soares EJ (2016) Viscoplastic dimensionless numbers. J Non-Newtonian Fluid Mech 238:57–64. https://doi.org/https://doi.org/10.1016/j.jnnfm.2016.05.001, URL https://www.sciencedirect.com/science/article/pii/S0377025716300465

[Wendell et al(2013)Wendell, Pigeonneau, Gouillart, and Jop] Wendell DM, Pigeonneau F, Gouillart E, et al (2013) Intermittent flow in yield-stress fluids slows down chaotic mixing. Phys Rev E 88(2):023,024

[Younes(2020)] Younes E (2020) Nouveau mélangeur à advection chaotique pour les fluides visqueux newtoniens et à seuil. PhD thesis, Nantes University, LTEN, France, URL http://www.theses.fr/2020NANT4020

[Younes et al(2022)Younes, Moguen, El Omari, Burghelea, Le Guer, and Castelain] Younes E, Moguen Y, El Omari K, et al (2022) Experimental study of chaotic flow and mixing of Newtonian fluid in a rotating arc-wall mixer. Int J Heat Mass Transfer 187:122,459